Post Shot Report: High-Convergence Implosions in Tetrahedral Hohlraums (ID4-FY98)

August 31 – September 4, 1998

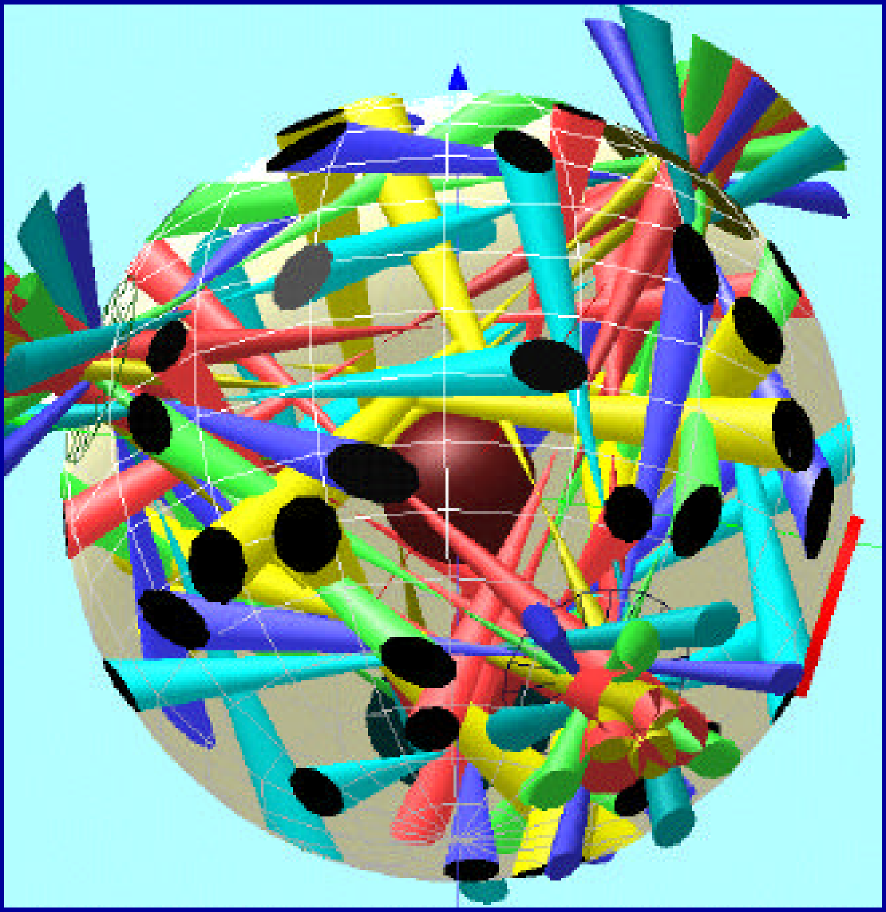

UR LLE

Los Alamos
Inertial Confinement Fusion

LA-UR-99-2044

Post Shot Report: High-Convergence Implosions in Tetrahedral Hohlraums

(ID4-FY98)

Thomas J. Murphy, Editor
Plasma Physics Group, P-24
University of California, Los Alamos National Laboratory
Los Alamos, NM 87545

LA-UR 99-2044

Post Shot Report: High-Convergence Implosions in Tetrahedral Hohlraums (ID4-FY98)

This document was prepared to allow timely distribution of preliminary analysis of a series of experiments. More extensive analysis may lead to changes in any conclusions reported here. This document is not to be cited in any external publication without permission of the authors.

This document was produced by the Los Alamos National Laboratory under the auspices of the United States Department of Energy under contract no. W-7405-ENG-36.

Introduction

The utility of the Omega laser facility for indirect-drive inertial confinement fusion experiments has been irrefutably demonstrated.$^{1-3}$ Experiments have demonstrated that cylindrical hohlraums using up to 40 of the 60 Omega beams can be used to produce symmetric implosions with shapes predictable by existing ICF codes.[2]

Experiments have also been performed[4,5] that utilize spherical hohlraums with a tetrahedral arrangement of laser entrance holes,[6,7] also known as "tetrahedral hohlraums." These experiments allow the use of all 60 Omega beams to drive implosions, and have potential symmetry advantages over cylindrical hohlraums. In the first set of experiments,[8] x-ray drive and implosion symmetry and performance were measured using spherical hohlraums with 2300-μm inside diameter (scale-1) with 1 ns square and shaped laser drives, and 2800-μm inside diameter (scale-1.2) with 1 ns square laser drive. Implosion images obtained through a laser entrance (LEH) hole showed a distinctive $m = 3$ component aligned with the LEHs.

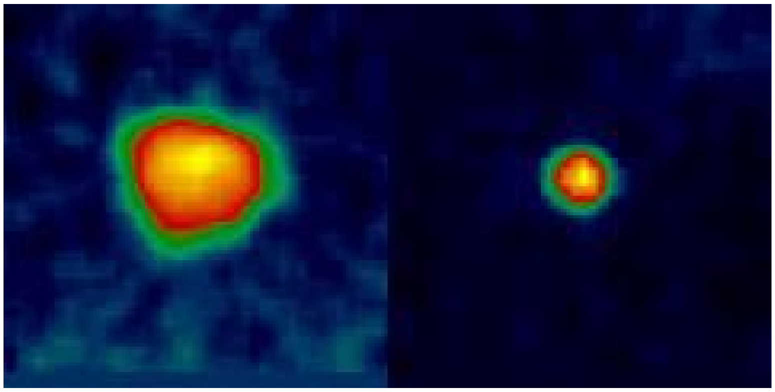

Figure 1: In the first set of tetrahedral experiments, implosion images contained a significant m=3 component (left), while larger hohlraums, smaller LEHs, and longer pulse shape reduced the $m = 3$ *component to negligible levels in a follow-up campaign (right).*

A follow-up set of experiments utilized scale-1.2 hohlraums with reduced laser entrance hole diameters and shaped laser pulses. The combination created implosion images with almost no $m = 3$ component in the shape. While fully-integrated three-dimensional calculations of the symmetry from an inherently three-dimensional experiment such as this are not available, simpler calculations indicate that these hohlraums produce a radiation drive with greatly reduced time-dependent asymmetry as compared to cylindrical hohlraums. Therefore, this configuration has the potential to allow implosion hydrodynamics experiments that do not have the complication of time-dependent drive asymmetry affecting the interpretation of the data.

In this experiment, we investigated the utility of tetrahedral hohlraums for:

- Driving capsules symmetrically in a time-dependent manner, allowing investigations of capsule hydrodynamics without the complication of time-dependent symmetry effects;
- Driving planar packages for witness-plate radiation temperature measurements and for weapons physics experiments.

During this set of experiments, we also activated two new Los Alamos diagnostics:

- Neutron bang time system capable of measuring the average time of neutron emission for targets yielding greater than 10^8 DD neutrons to an accuracy of 100 ps;
- An optical telescope was activated and demonstrated as a streaked optical pyrometer.

During the implosion experiment, two types of capsule were utilized. "Standard" plastic capsules were used in an experiment to measure the degradation of performance with increaing convergence. Double shell capsules were used to determine their potential as an alternate NIF ignition capsule design.

The detailed experimental plan was prepared and is available.[9]

Chapter 1

Pointing shot for tetrahedral pointing

Ken Klare's beam pointing calculations for a scale-1.2 tetrahedral hohlraum with 700-μm-diameter laser entrance holes was provided to LLE personnel for targeting each of the laser beams. Ken's spreadsheet provided LLE with X, Y and Z offsets in microns with respect to the centers of each of the LEHs. For the 4-mm-diameter precision pointing sphere, Ken also provided LLE with the appropriate defocus Z offset in order to produce sharp focus on the pointing sphere surface.

The pointing shot put 100 joules UV on target and was diagnosed using pinhole cameras in TIMS 2, 3, and 6 as well as the fixed pinhole cameras H9, 12, 3, 13, and P12. The pinhole cameras were at 4× magnification, used 5 μm pinholes with 5 mil beryllium filtering. Good enough data was obtained from all the pinhole cameras so that only one pointing shot was required. The data was scanned and reduced using the templates provided by Ken Klare and Jeremy Schnittman. Only three beams had offsets greater than 50 μm, and the mean offset for all 60 beams was 27 μm. It was felt that the pointing was adequately verified so that the planned double shell target shots could proceed with no further pointing shots. At the end of the day, LLE personnel retargeted the 4 beams with the largest offsets using dead reckoning in order to fine tune the pointing for the rest of the week's shots.

Figure 1.1, shows the TIM2 view of the spots on the pointing sphere. The circle about each spot is the expected position for each spot. The data shown in the figure is typical, although 2 spots were not seen at all in the H13 view.

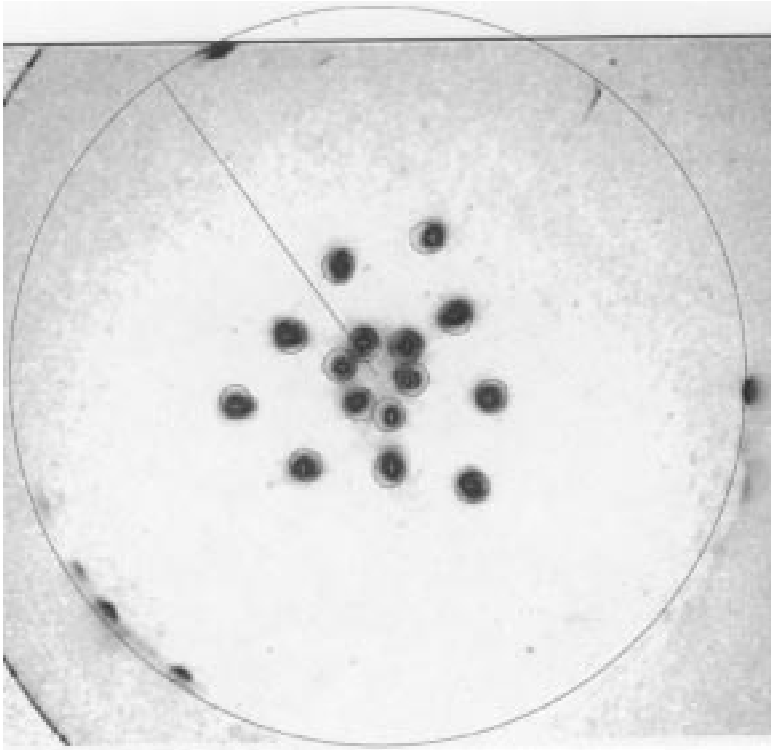

Figure 1.1: Results of a pointing sphere target shot.

Chapter 2

Double shell implosions

The double shell implosions done at Omega in August 1998 consisted of an inner glass microballoon (106 μm IR) filled with 36 atm of either DT or DD, surrounded by a foam region 69 μm thick and a outer solid CH shell 77 μm thick. The foam and outer solid CH shells were made from machined hemispheres glued together. These shots constituted a first attempt at Omega, using the inherently better time dependent thermal radiation field symmetry in a tetrahedral hohlraum, to study a potential non-cryogenic, high convergence NIF point design (CR ~38). The primary diagnostics on the shots (3 DT and 2 DD) were neutron yield, bang time, and burn history. An effort to use the Medusa array to monitor ion temperature and ρR produced no results due to the yield. Neutron yield was low on all shots, ranging from 0.6–2.0% of clean, based on a 30 kJ incident energy in the calculations, with 2 kJ assumed backscattered so that 28 kJ drove the target. This YOC result is essentially identical to earlier attempts to use a double shell design on Nova and earlier on Shiva, and suggest that the drive asymmetry differences between cylindrical and tetrahedral hohlraums, and the different beam energy balance in the facilities, is not the limiting factor in the poor implosion behavior. The results of the experiment are shown in Table 2.1. Figure 2.1 shows the typical power history delivered by the laser. Figure 2.2 shows the nominal target design, and Figure 2.3 is a Hyades 1-D hydro-code calculation showing the approximate implosion history expected during these shots.

An auxiliary diagnostic, backlit imaging of the capsule at early time utilizing the Au hohlraum wall emission, proved useful, showing evidence of both apparent azimuthal surface perturbations by about 700 ps, and of a perturbation probably associated with the joint between the hemispheres, on some shots. This imaging data may provide information useful in improving future double shell implosions. An image with several such features is shown in Figure 2.4.

Diagnostics on the first double shell experiments at Omega functioned well, given the design of those diagnostics. Unfortunately, the double shell yield was low enough to place severe strains on the capability of the neutron suite. If the yield of later target shots is higher due to correction of whatever is degrading the yield, the sensitivity problems may be self-correcting. However, if more targets are shot with yields in the region seen in the first set, it would be advisable to field more sensitive versions of the bang time detector and the burn history measurement (NTD). While the first of these may be satisfied by the LANL bang time detector, which was not online for the first day of the August 1998 tetrahedral campaign, the second (burn history) sensitivity increase will be difficult to achieve without

Table 2.1: Experimental results from the first Omega double shell shots. [a]Estimated using 30 kJ incident, 2 kJ backscattered. [b]One missing beam. [c]Estimated accuracy 50 ps due to low signal levels. Measured bang time is corrected by 200 ps to coincide with calculational definition of bang time.

Shot	Capsule	Energy on target (kJ)	YOC (%)	Predicted yield[a] $(\times 10^{10})$	Measured yield $(\times 10^{8})$	Bang time / burn duration[c] (ns)
13652	2-5DT RID4641	30.7	2.0	2.5	4.77 ± 0.23	2.109 / 0.145
13653	2-3DT RID4642	29.5[b]	1.6	2.5	4.22 ± 0.21	2.184 / 0.214
13655	2-2DT RID4643	31.0	1.0	2.5	2.39 ± 0.16	1.994 / 0.267
13658	1-2DD RID4643	30.2	0.6	0.06	0.039 ± 0.0031	NA
13661	1-5DD RID4648	29.7	1.2	0.06	0.069 ± 0.0036	NA

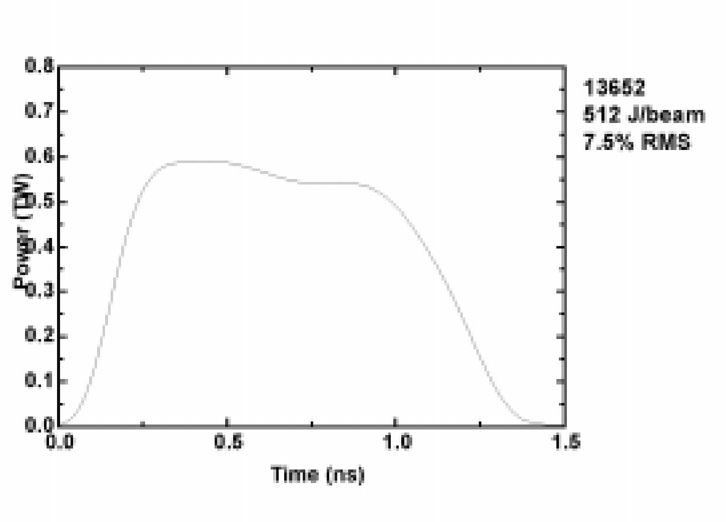

Figure 2.1: Typical delivered power history.

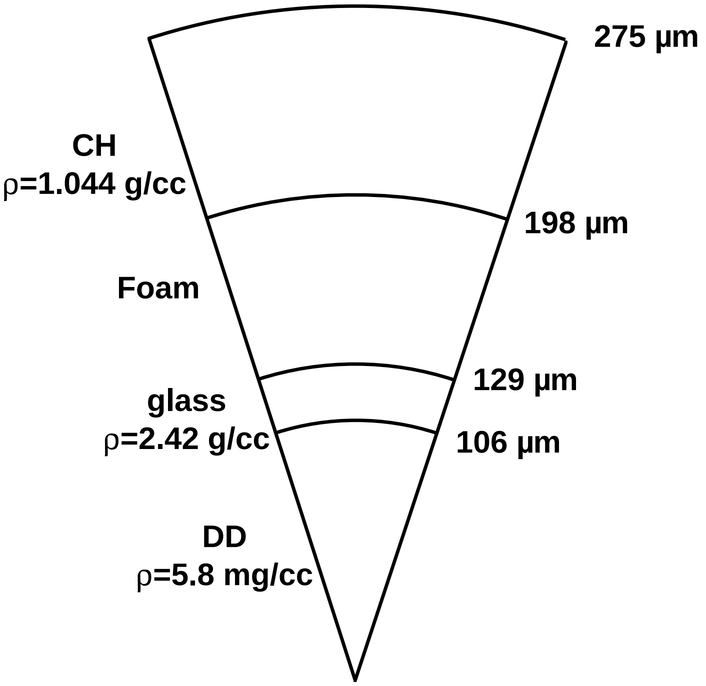

Figure 2.2: Nominal Omega double shell target design for the first series.

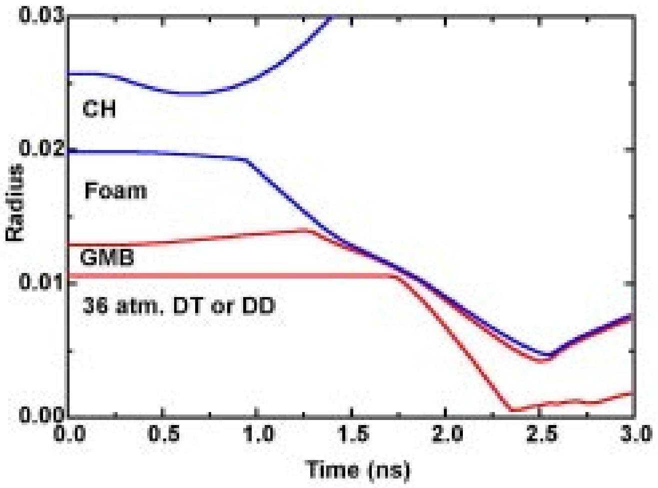

Figure 2.3: Hyades calculation of anticipated implosion history for the Omega shots.

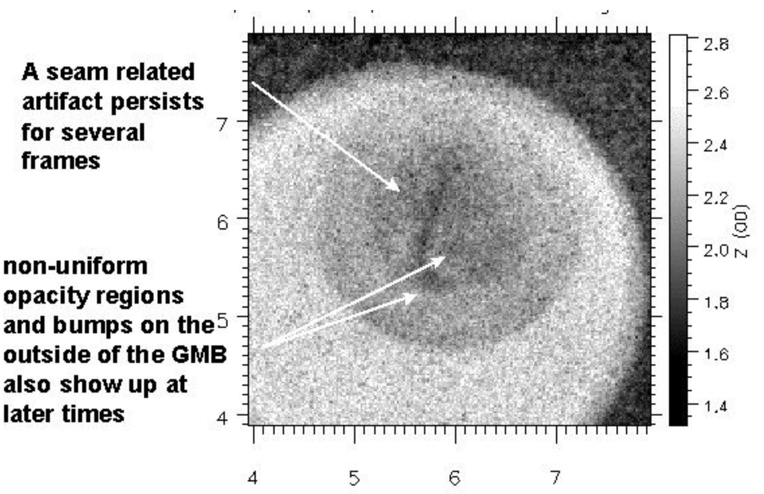

Figure 2.4: Image at 700 ps showing non-uniformities of several types seen with thermal radiation backlighting using the Au wall as a backlight source.

a completely new instrument, which is not currently planned. Implosion imaging of the double shells could be improved by use of an external, high-energy (4.7 keV Ti) backlighter to remove the obscuration from images after 800-900 ps seen in the initial experiments, caused by forelighting from Au between the capsule and the camera. Unfortunately, the loss of energy and symmetry inside the hohlraum due to missing beams used for such a backlighter source would further reduce the implosion characteristics. Consequently, it is far from obvious what diagnostic improvements could be made to the configuration for the next implosion series. Further consideration is being given to the diagnostic issues.

Because of the images and the essentially similar results from cylindrical and tetrahedral hohlraums, the inner glass microballoon and the foam + solid outer layers are being re-examined to determine whether any of the common target elements in the Nova and Omega experiments can be determined to be at fault for the poor results seen on all experiments done to date (over the last 20 years, in fact). Thus far, precipitated salts on the exterior of the GMB and non-uniform opacity regions in the glass seem to have been eliminated from consideration by target fabrication examination of similar capsules to those shot. A candidate that seems likely to account for the performance loss is non-uniform Au M-band radiation from under the laser spots that is able to penetrate the outer CH and foam (approximately 30% transmission of 2.5-keV radiation to the inner capsule occurs with the present pure CH outer 77-μm-thick shell). The next campaign at Omega may use either a pure-CH inner capsule to remove the capsule sensitivity to non-uniform preheat, or a doped outer ablator in place of the present CH to remove incident M band on the inner GMB. Both concepts are under analysis as ways of eliminating one prime contender for the cause of performance degradation.

Chapter 3

High-convergence implosions

3.1 Introduction

Although this experiment hinges upon successful neutron measurements (DD yield, ion temperature, DT yield, and DT energy spectra), a significant fraction of this summary focuses upon x-ray imaging because unlike neutron diagnostics, some near-term improvements are possible with the LLE x-ray framing cameras (XRFC's). Jon Wallace will be reporting the neutronic details in a similar but separate summary.

Thirteen high-convergence shots were obtained on 09/03/98, and many of the details are included in the following spreadsheets. Of particular note was the very low YOC's that the Ar-doped capsules returned. The source of this discrepancy (compared, say, to the LLNL Omega shots of April '98 where their similar Ar-doped capsules gave very reasonable YOC's) is not known, although it was almost certainly a target fabrication issue. An additional surprise was the very weak time-integrated x-ray images obtained, both pinhole and KB. For instance, on many shots the three independent x-ray diagnostics (20.3× KB3, 13× KB1, and one TIM-based plus six static 4× pinhole cameras) returned only the very faintest, if any, implosion images.

3.2 Highlights and ideas for March '99 series

Clearly these two surprises (one being a target fabrication issue, and the other being an expectation of tetrahedral implosions with LLE x-ray imaging instruments to behave similar to analogous Nova experiments with Nova diagnostics), are of lesser consequence in regard to the basic result, which is assuming scale-1.2 tetrahedral hohlraums provide much better time-dependent and time-averaged drive symmetry than their cylindrical counterparts, and that this is important to YOC's at high convergence, then the tetrahedral results are perhaps somewhat inconclusive, since the measured YOC's are rather similar to those of LLNL's Omega series of April '98. This raises the obvious question, is one really sure the presumed difference in drive uniformity qualities (cylindrical *vs.* tetrahedral) for these similar capsules designs (LLNL being Ge-doped, and LANL having undoped ablators), and similar convergence ratios, is important to the YOC? If it is not, then perhaps in both experiments the YOC fall-off with increasing convergence is largely hydrodynamic-instability limited. Clearly, if this hypothesis was experimentally proven, the implications would be very important indeed. On the other hand, if drive uniformity—not hydro instability—is the dominant effect, one is faced with the following questions:

1. Were the drive temperatures as expected, or were they somewhat lower because of some unforeseen energy loss mechanism—so leading to a artificially low YOC? This seems unlikely, as good Dante data was obtained in the previous tetrahedral hohlraum campaigns.
2. The tetrahedral drive is believed to contain a significant gold M-band component, so has the resulting pre-heat affected YOC's (and η's) detrimentally? This pre-heat source was neglected from the 1-D LASNEX calculations, but perhaps it is more important than first expected.
3. Is one certain the tetrahedral drive uniformity of 09/03/98 was as expected and superior to the 40 beam cylindrical hohlraum? Well, it's very difficult to believe it could have been worse than the cylindrical option! However, there is some evidence (Fig. 3.1) for a 25 atm DD implosion shot (#13673 viewed with KB3, a high spatial resolution x-ray microscope) that the time-integrated symmetry was 'triangular,' and that some refinements in hohlraum tuning (e.g. beams irradiating areas nearer to LEH rim, etc.), fabrication (e.g. LEH's located more precisely on each tetrahedral vertex), and LLE beam pointing accuracies are necessary.
4. Were sufficiently high convergence ratios probed? Perhaps the presumed tetrahedral advantage of improved drive uniformity only becomes apparent at very high convergences! In this vein, the YOC data that Jon Wallace will discuss in his companion report, may hint that YOC *vs.* convergence ratio has reached a plateau around $\eta = 15 - 20$.

These questions help define the next high-convergence experiment, for March '99. For instance:

1. The experiment will precede a LLNL indirect-drive week; therefore Robert Turner will be preparing Dante and we should coordinate with him so we obtain the best possible radiation temperature measurements. Additionally, we will request the backscatter diagnostic to be running (the contact person being Wolf Seka).
2. Ge-doped capsules will be used to reduce M-band pre-heat effects, and at the same time increase the DD and DT yields for improved ion temperature and nuclear ρR measurements, respectively. The use of thinner ablator shells, with similar DD fill pressures, will also contribute to increased DD and DT yields and convergence ratios.
3. The same scale-1.2 hohlraum will be retained; however, target fabrication will be requested to make extraordinary efforts in correctly locating the LEH's. In addition, Jon Wallace will be "generalizing" his view factor code to model the effects of slightly misplaced entrance holes of the 09/03/98 targets. LLE is continually improving their

pointing procedures, and so we may request permission to place beams closer to LEH's edges (from 100 to 50 μm, say). Also, perhaps two pointing shots rather than just one is important?

4. Finally, higher convergence ratio, Ge-doped, capsules will be used for a fraction of the shots. Also, if LLNL provide to us $\sim$10 of their Omega cylindrical hohlraum characterized high-convergence capsules, we could implode these within tetrahedrals to make a definitive comparison between the two hohlraums.

As an aside, Jon Wallace has made an interesting observation regarding the LASNEX calculation of DD yield for Ge-doped capsules and experiment; i.e. there appears to be some artifact inherent to LASNEX which underestimates yield quite significantly. Thus, if we had used Ge doping on 09/03/98, the YOC's may have been somewhat higher. Clearly, the use of Ge-doped ablators will have several advantages for the March '99 tetrahedral series.

3.3 X-ray imaging improvements

For the March '99 series, the use of Ge-doping may reduce x-ray brightness due to the increased ablator opacity. However, we will continue to direct maximum effort towards improved x-ray imaging, even though neutronics will remain the principle diagnostic. Perhaps the two most interesting events from an x-ray imaging perspective are: (1) the capsule symmetry at the point in time where the laser pulse has ended and the hohlraum is cooling down (several hundred ps prior to bang time); and (2) the capsule condition at the precise point of neutron production (slightly earlier than the peak x-ray emission event). The former is important because the integrated effects (or damage done) of drive asymmetries are over, but the capsule is still large enough to usefully study. The latter, with images of sufficient spatial resolution and signal-to-noise quality, may allow one to correlate capsule symmetry with YOC. We attempted (2), but the presumed correlation is difficult to identify because of extremely poor signal-to-noise ratios (S/N) from the 12× magnification x-ray framing camera (XRFC4). An additional but much lesser complication in this case, is that as a perfectly spherical implosion target approaches a diameter within an order of magnitude or so of the spatial resolution scale, a non-circular pinhole will project a non-circular image no matter which exposure contour is taken. The consequence being, a 4×4 pinhole array consisting of randomly shaped 5-μm mean diameter holes will produce 16 randomly shaped implosion images, even if the target is perfectly spherical. Such misleading effects can be mitigated by using circular pinholes of course, and/or improving spatial resolution (smaller pinholes). However, we stress here that very poor S/N was by far the dominant effect here.

3.3.1 Time-Integrated

Of the three x-ray imaging instruments used, the 4× pinhole cameras had the largest collection efficiency ($\Delta\Omega \approx 1.7 \times 10^{-10}$). KB3 had a larger subtending solid angle ($\Delta\Omega \approx 1 \times 10^{-7}$), but the 20.3× magnification and energy-dependent mirror reflectivity folded in to produce

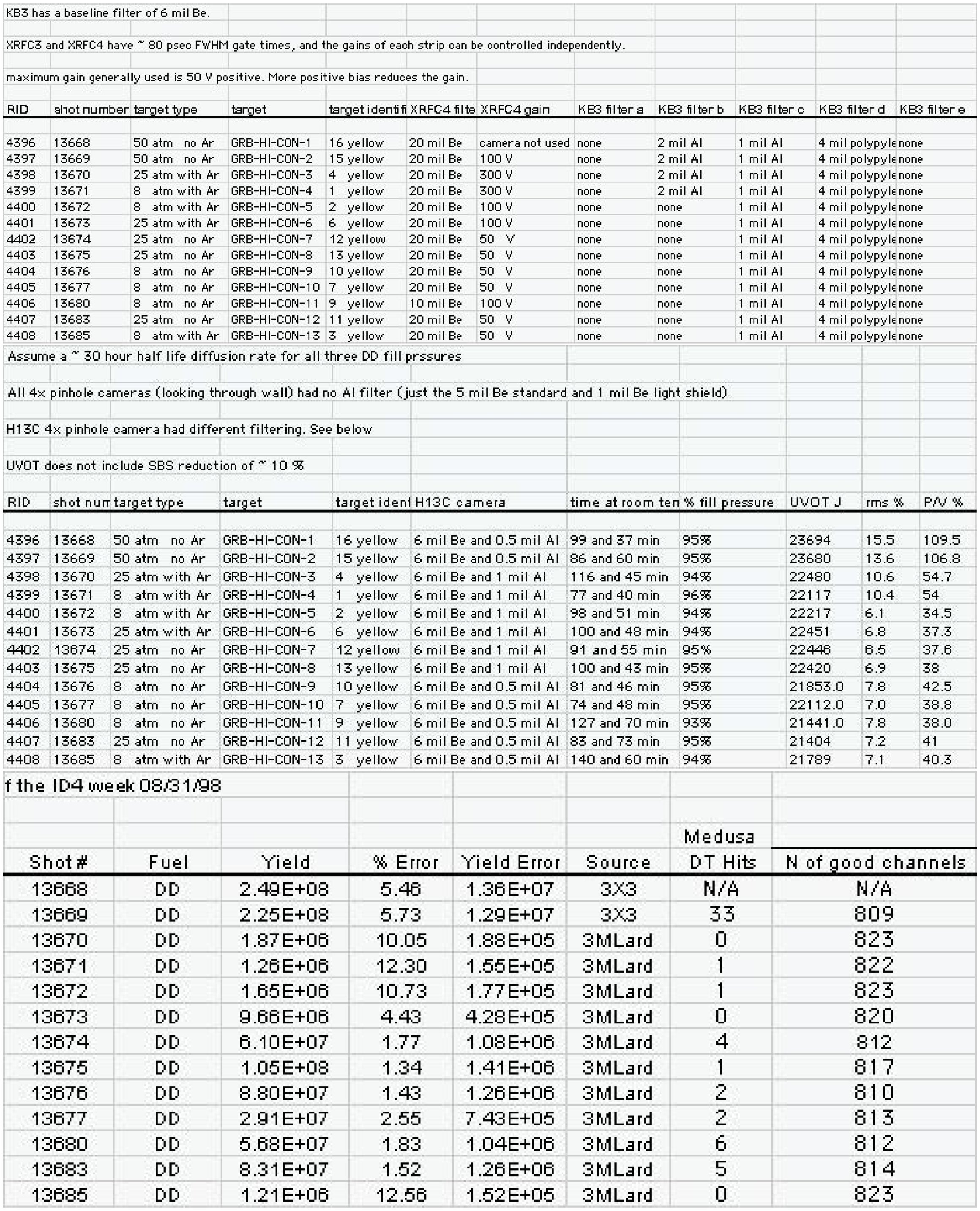

KB3 has a baseline filter of 6 mil Be.

XRFC3 and XRFC4 have ~ 80 psec FWHM gate times, and the gains of each strip can be controlled independently.

maximum gain generally used is 50 V positive. More positive bias reduces the gain.

RID	shot number	target type	target	target identifi	XRFC4 filte	XRFC4 gain	KB3 filter a	KB3 filter b	KB3 filter c	KB3 filter d	KB3 filter e
4396	13668	50 atm no Ar	GRB-HI-CON-1	16 yellow	20 mil Be	camera not used	none	2 mil Al	1 mil Al	4 mil polypyle	none
4397	13669	50 atm no Ar	GRB-HI-CON-2	15 yellow	20 mil Be	100 V	none	2 mil Al	1 mil Al	4 mil polypyle	none
4398	13670	25 atm with Ar	GRB-HI-CON-3	4 yellow	20 mil Be	300 V	none	2 mil Al	1 mil Al	4 mil polypyle	none
4399	13671	8 atm with Ar	GRB-HI-CON-4	1 yellow	20 mil Be	300 V	none	2 mil Al	1 mil Al	4 mil polypyle	none
4400	13672	8 atm with Ar	GRB-HI-CON-5	2 yellow	20 mil Be	100 V	none	none	1 mil Al	4 mil polypyle	none
4401	13673	25 atm with Ar	GRB-HI-CON-6	6 yellow	20 mil Be	100 V	none	none	1 mil Al	4 mil polypyle	none
4402	13674	25 atm no Ar	GRB-HI-CON-7	12 yellow	20 mil Be	50 V	none	none	1 mil Al	4 mil polypyle	none
4403	13675	25 atm no Ar	GRB-HI-CON-8	13 yellow	20 mil Be	50 V	none	none	1 mil Al	4 mil polypyle	none
4404	13676	8 atm no Ar	GRB-HI-CON-9	10 yellow	20 mil Be	50 V	none	none	1 mil Al	4 mil polypyle	none
4405	13677	8 atm no Ar	GRB-HI-CON-10	7 yellow	20 mil Be	50 V	none	none	1 mil Al	4 mil polypyle	none
4406	13680	8 atm no Ar	GRB-HI-CON-11	9 yellow	10 mil Be	100 V	none	none	1 mil Al	4 mil polypyle	none
4407	13683	25 atm no Ar	GRB-HI-CON-12	11 yellow	20 mil Be	50 V	none	none	1 mil Al	4 mil polypyle	none
4408	13685	8 atm with Ar	GRB-HI-CON-13	3 yellow	20 mil Be	50 V	none	none	1 mil Al	4 mil polypyle	none

Assume a ~ 30 hour half life diffusion rate for all three DD fill prssures

All 4x pinhole cameras (looking through wall) had no Al filter (just the 5 mil Be standard and 1 mil Be light shield)

H13C 4x pinhole camera had different filtering. See below

UVOT does not include SBS reduction of ~ 10 %

RID	shot num	target type	target	target ident	H13C camera	time at room ten	% fill pressure	UVOT J	rms %	P/V %
4396	13668	50 atm no Ar	GRB-HI-CON-1	16 yellow	6 mil Be and 0.5 mil Al	99 and 37 min	95%	23694	15.5	109.5
4397	13669	50 atm no Ar	GRB-HI-CON-2	15 yellow	6 mil Be and 0.5 mil Al	86 and 60 min	95%	23680	13.6	106.8
4398	13670	25 atm with Ar	GRB-HI-CON-3	4 yellow	6 mil Be and 1 mil Al	116 and 45 min	94%	22480	10.6	54.7
4399	13671	8 atm with Ar	GRB-HI-CON-4	1 yellow	6 mil Be and 1 mil Al	77 and 40 min	96%	22117	10.4	54
4400	13672	8 atm with Ar	GRB-HI-CON-5	2 yellow	6 mil Be and 1 mil Al	98 and 51 min	94%	22217	6.1	34.5
4401	13673	25 atm with Ar	GRB-HI-CON-6	6 yellow	6 mil Be and 1 mil Al	100 and 48 min	94%	22451	6.8	37.3
4402	13674	25 atm no Ar	GRB-HI-CON-7	12 yellow	6 mil Be and 1 mil Al	91 and 55 min	95%	22446	6.5	37.6
4403	13675	25 atm no Ar	GRB-HI-CON-8	13 yellow	6 mil Be and 1 mil Al	100 and 43 min	95%	22420	6.9	38
4404	13676	8 atm no Ar	GRB-HI-CON-9	10 yellow	6 mil Be and 0.5 mil Al	81 and 46 min	95%	21853.0	7.8	42.5
4405	13677	8 atm no Ar	GRB-HI-CON-10	7 yellow	6 mil Be and 0.5 mil Al	74 and 48 min	95%	22112.0	7.0	38.8
4406	13680	8 atm no Ar	GRB-HI-CON-11	9 yellow	6 mil Be and 0.5 mil Al	127 and 70 min	93%	21441.0	7.8	38.0
4407	13683	25 atm no Ar	GRB-HI-CON-12	11 yellow	6 mil Be and 0.5 mil Al	83 and 73 min	95%	21404	7.2	41
4408	13685	8 atm with Ar	GRB-HI-CON-13	3 yellow	6 mil Be and 0.5 mil Al	140 and 60 min	94%	21789	7.1	40.3

f the ID4 week 08/31/98

Shot #	Fuel	Yield	% Error	Yield Error	Source	Medusa DT Hits	N of good channels
13668	DD	2.49E+08	5.46	1.36E+07	3X3	N/A	N/A
13669	DD	2.25E+08	5.73	1.29E+07	3X3	33	809
13670	DD	1.87E+06	10.05	1.88E+05	3MLard	0	823
13671	DD	1.26E+06	12.30	1.55E+05	3MLard	1	822
13672	DD	1.65E+06	10.73	1.77E+05	3MLard	1	823
13673	DD	9.66E+06	4.43	4.28E+05	3MLard	0	820
13674	DD	6.10E+07	1.77	1.08E+06	3MLard	4	812
13675	DD	1.05E+08	1.34	1.41E+06	3MLard	1	817
13676	DD	8.80E+07	1.43	1.26E+06	3MLard	2	810
13677	DD	2.91E+07	2.55	7.43E+05	3MLard	2	813
13680	DD	5.68E+07	1.83	1.04E+06	3MLard	6	812
13683	DD	8.31E+07	1.52	1.26E+06	3MLard	5	814
13685	DD	1.21E+06	12.56	1.52E+05	3MLard	0	823

Table 3.1: Neutron diagnostic results (Vladimir Glebov's spreadsheet).

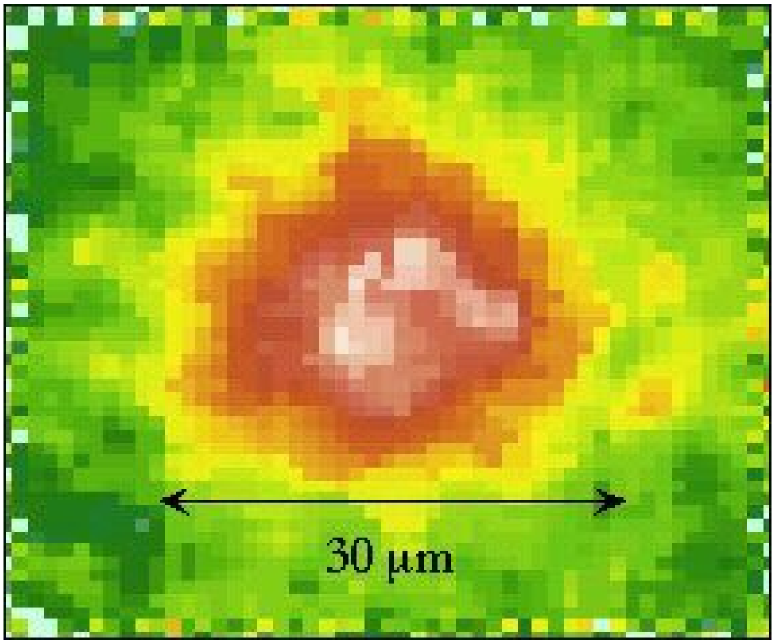

Figure 3.1: Time-integrated x-ray image of implosion shot #13673 using KB3; a high spatial resolution microscope. Each pixel is 0.99 μm. Unequal magnifications in two resolving planes has not been allowed for yet (a very small effect). Median filter of 7 pixels in width (~7 μm) has been used to smooth the ~3 μm spatial resolution image. Approximate 'triangular' shape does seem to correlate with LEH positions.

a less collection efficient system. KB1, a larger solid angle system ($\Delta\Omega \approx 4 \times 10^{-7}$), with 13× magnification and a dispersing grating, was about the same as KB3, although for 09/03/98, it looked through the hohlraum wall to produce very limited images. KB3, on the other hand, looked (almost) directly through the LEH aligned with H13; and so we were quite excited that the time-integrated images would be very interesting, since it has a high ~3 μm spatial resolution (this instrument will also map a spherical object into a non-circular image, but to a much lesser extent than a large pinhole). However, for all but one shot (#13673) the images collected were either non-existent or too faint, and therefore too noisy, to usefully use. Incorrect filtering was not the problem; two channels were filtered 'soft' (6 mil Be), one was medium (6 mil Be + 4 mil polypylene), and the fourth was hard (6 mil Be + 1 mil Al). For each shot, the first two were always overexposed, the third was perfect, and the fourth was too faint. The problem was quite simply insufficient x-ray flux, and so the necessity of a more sensitive time-integrated detector is clearly apparent; e.g. an x-ray CCD. Such a detector would not necessarily compromise spatial resolution if the pixels were ~25 μm or smaller.

In contrast, the 4× pinhole camera images were more plentiful—because they are more sensitive and there are more of them. However, with 10 μm mean pinhole diameters their data is perhaps less interesting because the spatial resolution scale is only a few times less than the feature being imaged. Suggesting, non-circular pinhole effects could become important. For March '99 the obvious improvements with time-integrated imaging are:

1. Attach a LANL x-ray CDD to KB3.
2. Convert the 4× TIM based pinhole camera such that magnification and collection solid angle are significantly increased; i.e. dramatically reduce object-to-pinhole distance, while significantly reducing the pinhole to film displacement.

In comparison to (2), the first suggestion could return very important data, and the temporary modification would be much simpler to implement. Due to limited photon fluxes, removing the MCP from GMXI/KB2 and attaching to KB3, would be not be an interesting choice.

3.3.2 Time-Resolved

The primary time-resolved x-ray imaging instrument was XRFC4, at 12× , located in TIM2 and looking through LEH B (aligned with H7). The 5 μm pinholes placed 351 mm from the MCP image plane resulted in a $\Delta\Omega = 1.6 \times 10^{-10}$ collection solid angle. This diagnostic was intended to image the capsule condition at or very near the neutron production instant, and therefore establish a possible correlation with capsule condition and YOC. Unfortunately, the S/N quality proved unacceptable, and at the time of writing no correlation has been determined. The noise originates from Poisson distributed MCP 'spikes,' an effect resulting from the very high gain (+50 V bias), the highest LLE generally uses. Reduced +100 V gain with the same filtering proved to be even worse for S/N. Although the noise spikes are easily identified along an image free MCP strip, the combination of real signal with such artifacts is impossible to distinguish. Therefore, one can never know if a feature on an implosion image is real or if it is simply noise. To this end, we either have to improve collection efficiency at 12× (e.g. larger pinhole) and reduce gain, and/or change the noise spectrum such that the spikes are less likely to superimpose features or blotches onto an image. For instance, with the same pinhole collection efficiency and noise spectrum, but significantly increased magnification, the effective S/N quality will improve approximately proportionally. Indeed, in the limit of higher magnifications the area of each spike will tend to zero and S/N will tend to infinity. Fortunately, the 6 mm wide MCP strips are much larger than the ∼0.6 mm diameter implosion images, implying a magnification increase by a factor of < 10 is possible; i.e. $< 120\times$. Furthermore, the resulting decrease in solid angle is only ∼0.87 of the 12× case. Clearly, the 10-times finer scale in the noise distribution would offset a 13% reduction in signal. 120× is of course too ambitious, as one could never hope to align the capsule, pinhole array, and MCP to the necessary accuracy; however, we believe 60× is a realistic option, in which case, the target-mounted pinhole array would be located ∼6.23 mm from the capsule, and the collection solid angle would be reduced to ∼0.88 of the standard 12× magnification. Mounting the pinholes to the necessary tolerances could be a major target fabrication difficulty. For example, a misplacement of the capsule and pinhole in opposite directions each by 25 μm, would lead to an unacceptable ∼3 mm image misalignment upon an MCP strip. However, ∼15 μm may be quite satisfactory; i.e. a ∼1.8 mm maximum displacement.

3.4 Obtaining higher drive temperatures in scale 1.2 hohlraums

In the quest for higher drive temperatures in scale 1.2 hohlraums, using the same PS22 pulse shape, the beams could be split and temporally staggered, by 1.1 ns, into two groups of 20 and 40. Each group running different ∼1.1 ns pulse shapes for maximum UV conversion efficiency such that PS22 is obtained but at a higher energy. Simple view factor calculations will quickly determine whether drive symmetry is adversely compromised for the modest energy gain.

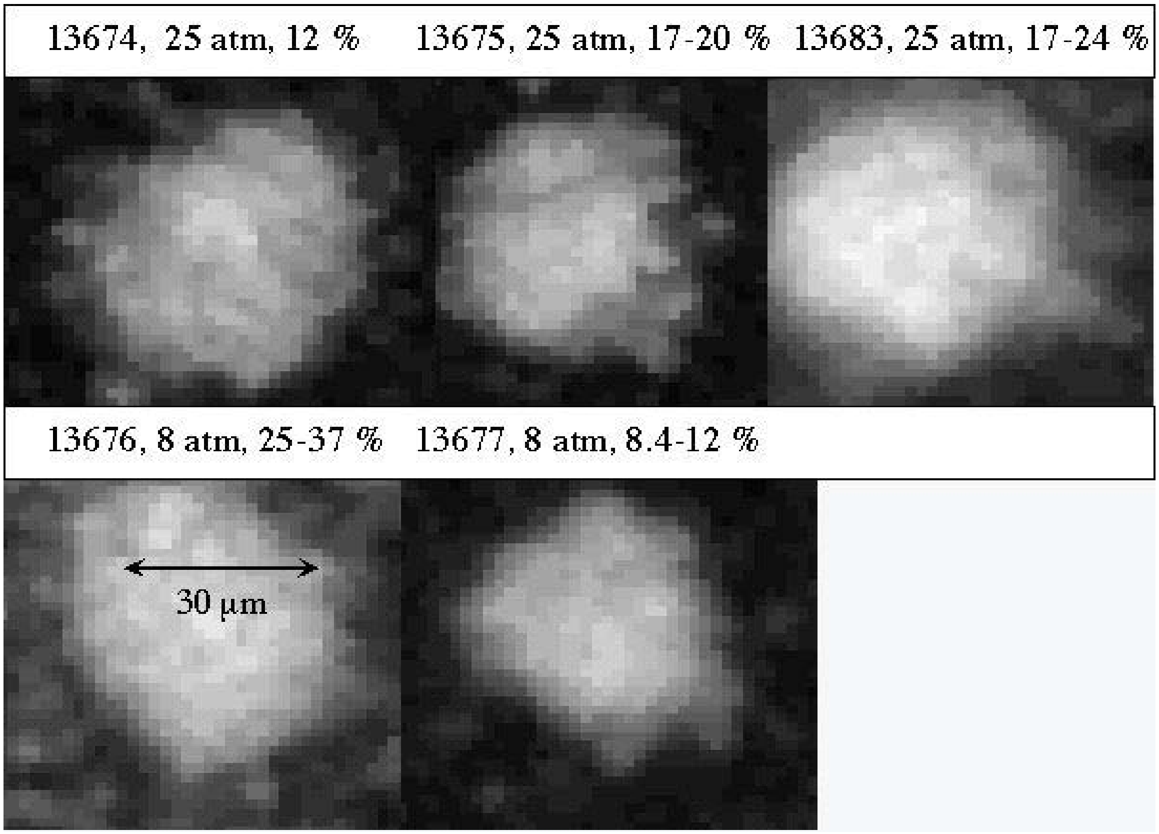

Figure 3.2: Capsule images at the instant of approximate neutron bang time. Data has been median filtered with a relatively large 8.33 μm width (each pixel corresponds to 20/12 = 1.67 μm). All shots do not contain Ar dopant. Percentage values refer to YOC. 50% exposure contours on film have been studied, but because of the very poor S/N, a symmetry analysis with contours of 45%, 55%, 60%, etc. yield very different results.

Chapter 4

Planar experiments

4.1 Introduction

Although tetrahedral hohlraums have been used on previous campaigns, little has been measured in terms of the drive strength and the usefulness of this geometry for structured-shock-wave physics (SSWP). These shots are the first of this series of SSWP on Omega with the objectives:

- Measuring the drive with Tetrahedrally Illuminated spherical hohlraums using Dante,
- Testing the SOP diagnostic implementation for target temperature history,
- Using the SOP with a witness plate to measure the spatial uniformity of the drive, especially looking for edge effects from the exit hole, and
- Using the SOP to find if a real target package can be diagnosed.

Two shots were executed on 09/02/98 and a further 9 shots were obtained on 09/04/98. We note that:

- We were able to measure the history of the drive using wedges and the SOP diagnostic,
- that Dante failed due to improper use (only two channels were recorded),
- that the spatial resolution of the SOP was not sufficient to observe a 20-μm wide structured shock,
- that the new Cone/Shield design worked well,
- and that pointing and focusing were well in hand and no laser beam hit any of the apertures or the conical shield.

This review covers the following topics:

- Experimental Design

- Uniformity Results From Flat Witness Plates:
    - Aluminum
    - Copper-Doped Beryllium
- Shock Velocity Measurements Using Steps
- Shock Velocity Measurements Using Wedges
- Discussion of Theoretical Drive Results
- Results from Structured Targets
- Summary
- Appendix-1 Preliminary Quick Post Shot Report On Operations.

4.2 Experimental design

A photograph of an assembled target is shown on Figure 4.1. The shield diameter was chosen to block ultraviolet emission (defined by the pass-band of the SOP filter) from the laser entrance holes and the ablation plume that ensues. It was too thin to block the x-ray preheat of the load. The design of the hohlraum and the conical shield are shown in Figure 4.2. The hohlraum had an internal diameter of 2800 μm and a gold thickness of 2 μm, sufficiently smaller than the Marshak depth for 2 ns illumination.

The laser beams enter the hohlraum through 4 holes arranged on the apex of a tetrahedron. Each laser entrance hole has a diameter of 700 μm, calculated to stay open during the 2 ns drive. The beams were focused at the laser entrance holes and arranged to provide uniform reradiation of the x-rays on a capsule within some of the hohlraums, and designed to miss the expansion of the same capsule. We used the same design for the present studies, this minimized the repointing and refocusing of the laser beams. For some of the shots we used 45 beams, thus selecting the other 15 beams to later provide illumination of iron or titanium backlighters. An example of this use is shown in Figure 4.1, where an iron foils covers one of the laser entrance holes, and will be used later as a backlighter for face-on radiography of foils or targets mounted on the SOP exit hole. The loads and witness plates are glued to a separate hole of diameter 700 μm that faces the SOP direction. An aluminized mylar conical shield is glued to the outside of the witness plate, giving a light-tight seal at the joint. The expected temperature in the gold-walled hohlraum, using scaling laws that worked on Helios with CO_2 lasers, and on Nova using Nd:Yag or Nd:Glass lasers, are shown in Figure 4.3. Using an aluminum witness plate it was expected that the shocks would be driven at a speed of 55 μm/ns (55 km/sec), with a peak pressure of 45 Mbar using a square laser pulse.

We faced two conflicting requirements: for SSWP we needed as much energy as possible to drive the shocks, but also needed sufficient laser energy to produce x-ray backlighting. We

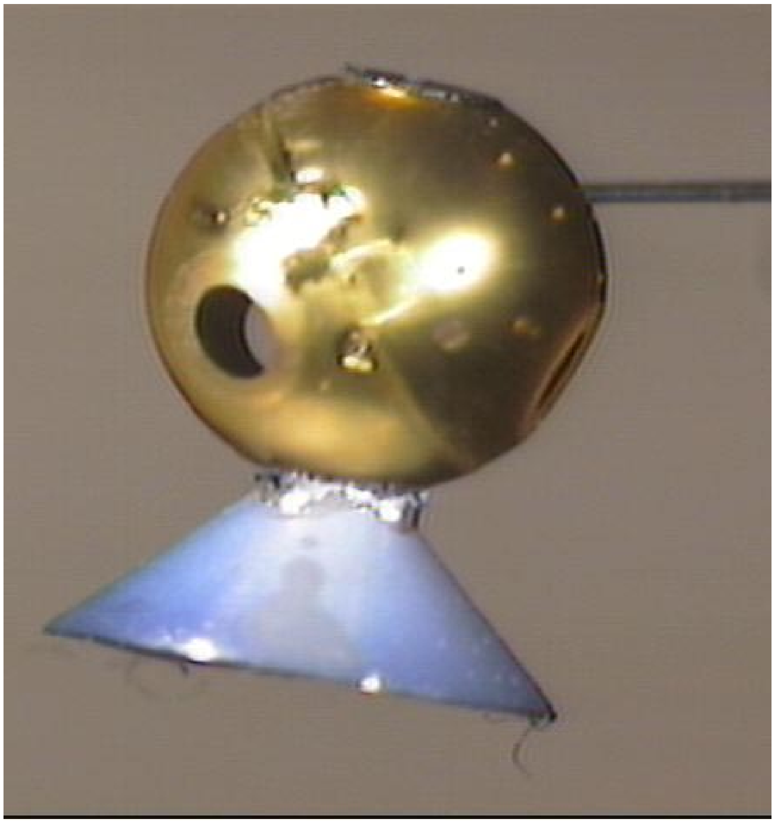

Figure 4.1: Photograph of a target showing cone, laser entrance holes, and an axial iron backlighter foil on the top of the picture.

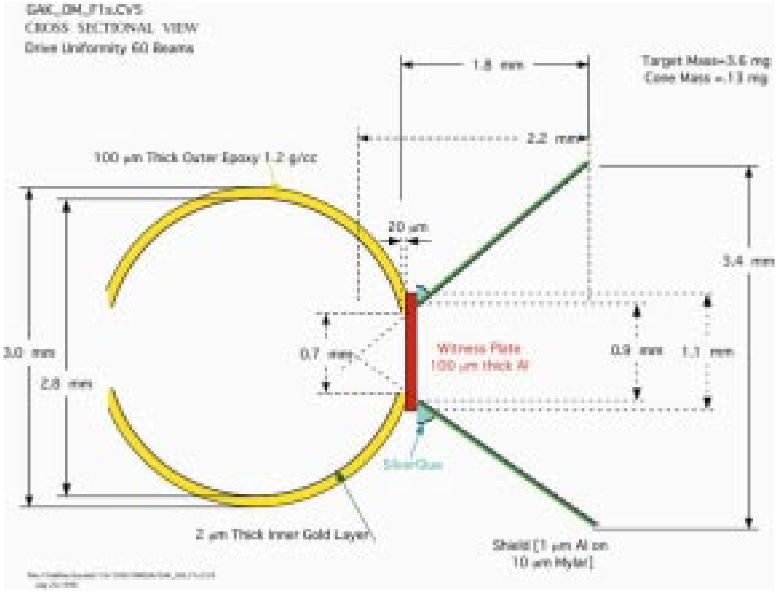

Figure 4.2: Schematic diagram of the target with a witness plate and a conical shield for the SOP diagnostic.

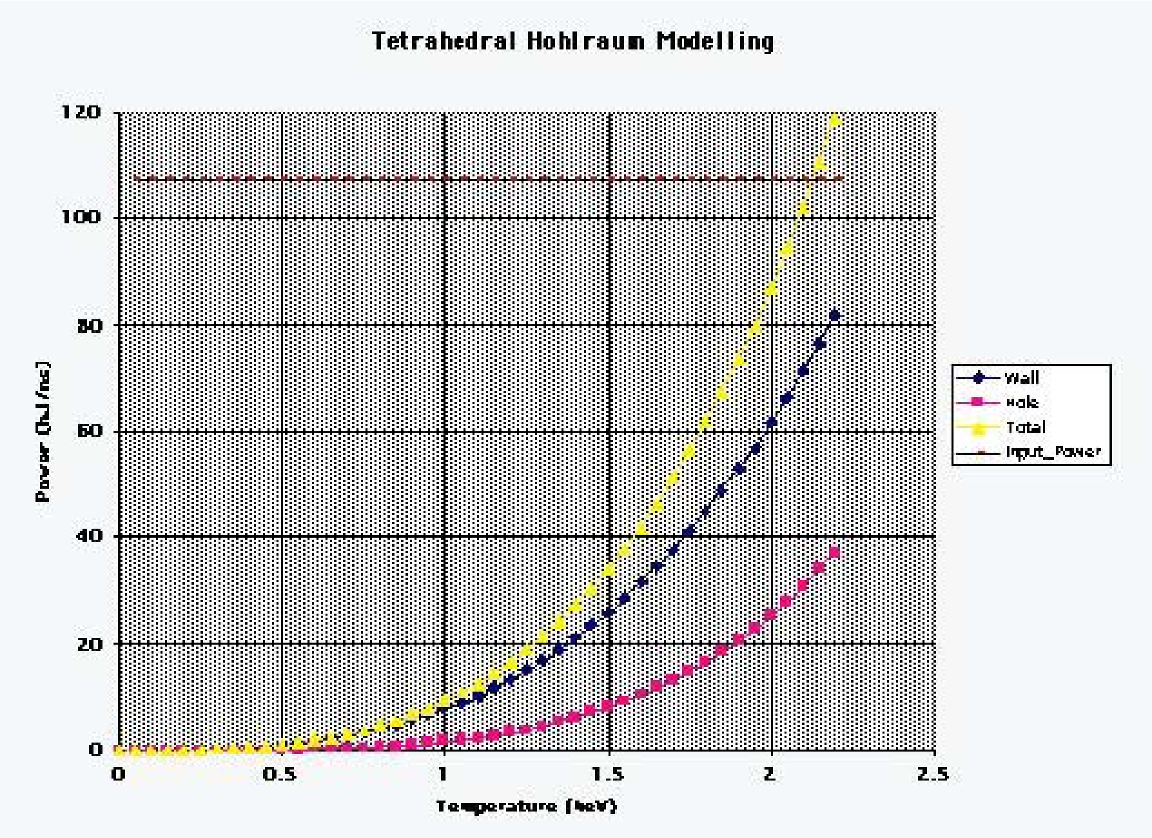

Figure 4.3: Hohlraum temperature vs temperature for 21.5 kJ incident and 90% absroption.

estimated that at least 10 beams (4.5 kJ of 3ω light) will be needed to register an image of a 500-μm-thick C_8H_7Cl target on an X-ray Framing Camera set at medium gain and with a magnification of 10 using an iron He-α like backlighter. The second conflict is that of using a sufficiently large shock front *vs.* having as uniform a shock as possible.

If the SOP can measure the spatial variation in the shock front distribution, then x-ray backlighting may not be needed. If the SOP fails, then ten beams must be used for radiography, reducing the drive. The design required two sets of measurements: one with all the beams, and one with a reduced set. Although the laser beam footprints may different in such cases, the full (60 beams) set may also give a useful drive measurement for implosion studies.

The main diagnostics for these experiments were:

- the SOP in port H14,
- the x-ray framing cameras XRFC3/SXRFC in port P3,
- Dante in location H16.

Secondary diagnostics were:

- x-ray pinhole cameras XRPHC1/P12A, XRPC2/H18c, XRPC3/H3c, XRPHC4/H13c, XRPHC5/H12c, XRPC#6 all set at magnifications of 4X
- X-ray framing camera XRFC2 in port P6
- P510 a and b streak cameras to measure the laser pulse shape

Plasma calorimeters scatttered around the chamber were also recorded. A summary of the SOP results is shown in Table 4.1, the details will be discussed in the coming sections. A summary of some of the "square" laser pulse shapes is shown after it in Figure 4.4.

4.3 Uniformity results from flat witness plates

4.3.1 Aluminum

100-μm-thick aluminum witness plates were used to test the uniformity of the drive. The witness plate covered the hole facing the SOP diagnostic. The plates were shielded by aluminum cones that were covered with plastic. This reduced the scattered light and shielded the SOP from the light emission from the laser entrance holes. The cone extended 100 μm beyond the projected circumference of the hohlraum. With 60 beams, shots 13662 and 13663 (30 and 23.85 kJ, respectively) produced a uniform shock of 600 μm diameter arrival times varying less than 20 ps for transit times of about 800 ps and 1536 ps, respectively. This corresponds to a uniformity of pressure of 2.5 and 1.25 % respectively. When we used 45 beams, with a drive energy of 21.4 kJ, a similarly uniformity region was produced. An example of the emission uniformity is shown in Figure 4.5.

Table 4.1: Summary of SOP results, and position of the start of the light emission.

Zero	-197	Pixels	Assumed beginning of laser pulse
Dp	5.37	ps/pixel	From Trident Calibration
Dn	186.2	Pixel/ns	From Dp

Shot #	P_0 Pixel	P_1 Pixel	T_0 ns	T_1 ns	Δt ns	Thick μm	Velocity μm/ns	Energy kJ	Comment
13662	-197	-47	-1.058	-0.252	0.806	100.3	124.52	30.00	Al flat 60 beams Just too much?
13663	-197	89	-1.058	0.478	1.536	101.5	66.09	23.85	Al Flat 60 beams
13689	-197	74	-1.058	0.397	1.455	100	68.72	21.40	Al Flat 45, Z to 1st light Assume 2nd is leakt
13689	74	422	0.397	2.266	1.869	100	53.51	21.40	Al Flat 45, 1st light to 2nd light assume
13689	-197	422	-1.058	2.266	3.324	100	30.08	22.40	Al Flat Zero to second pulse assume first leak
13690	-197	182	-1.058	0.977	2.035	50.1	24.62	21.60	Aluminum Ramp Base thickness 50 microns
13691	-197	120	-1.058	0.644	1.702	52.6	30.90	21.49	Alum Step Base
13691	120	370	0.644	1.987	1.343	74.7	55.64	21.49	Alum Step first
13691	370	750	1.987	4.028	2.041	74.7	36.61	21.49	Alum Step Second
13692	-197	212	-1.058	1.138	2.196	120	54.64	20.97	Be(Cu) Flat 45 beams 5-10% by wt Cu
13693	-197	206	-1.058	1.106	2.164	120	55.45	20.80	Be(Cu) Joint 45 beams at fraction 1/7 of Be
13694	-197	66	-1.058	0.354	1.412	50.4	35.69	21.34	Al Ramp Base
13695	-197	164	-1.058	0.881	1.939	52.1	26.88	21.20	Al Step Base
13695	164	370	0.881	1.987	1.106	75	67.80	21.20	Al Step First
13695	370	766	1.987	4.113	2.127	74.9	35.22	21.20	Al Step Second
13696	-197	210	-1.058	1.128	2.186	120	54.91	21.26	Be(Cu) Flat
13697	-197	47	-1.058	0.252	1.310	25	19.08	1.40	CH2 (3 beams)

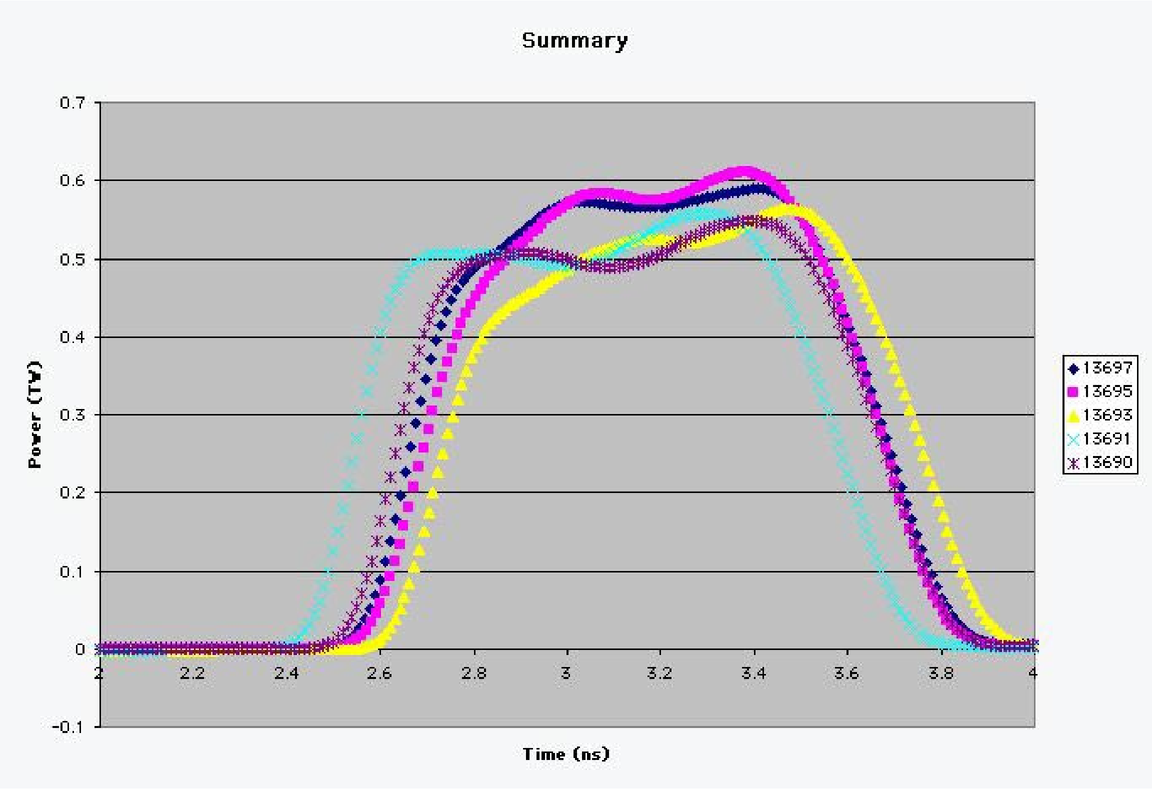

Figure 4.4: A collection of different delivered "square pulses" at different power levels. The shot numbers are shown at the right of the figure.

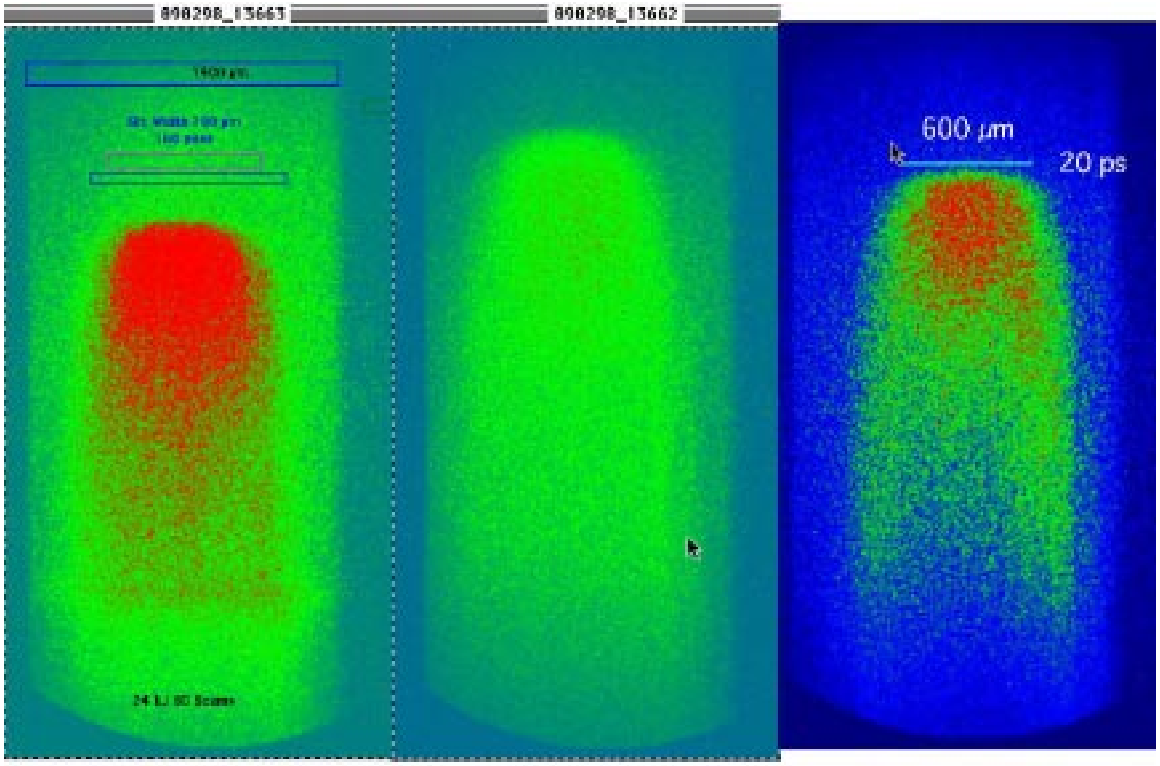

Figure 4.5: Uniformity of drive. Left and middle using 60 beams at two different energy levels with an aluminum witness plate. Right, shot 13694, using BeCu plate with 45 beams. The scale gives an idea of the sizes. The time axis is vertical starting at the top. Full scale is ∼5 ns.

4.3.2 Copper-doped Be

The transit time across 125 μm thick Cu-doped Be witness plates, shots 13692 and 13696, also showed a similar uniform region. The transit time, however, while consistent among the shots, gave a shock speed that is slower than that under similar conditions with an aluminum witness plate. It is expected that, for a non preheated target, the shock velocity driven by an ablation front should be proportional to the $\sqrt{1/\text{density}}$. We do not observe such a behaviour, suggesting some other mechanisms that drive the shock or preheat the targets. A possible source is preheat from the M-band emission of gold. The M-band was observed in the pinhole images as emission from the laser footprint inside the hohlraum.

4.4 Shock velocity measurements using steps

Two stepped aluminum targets were used in shots 13691 and 13695 with 45 beams. The shape and specification for the step are shown in Figure 4.6. Equal steps of 75-μm height were used. The wedge was displaced 100 μm vertically such that the rarefaction wave from

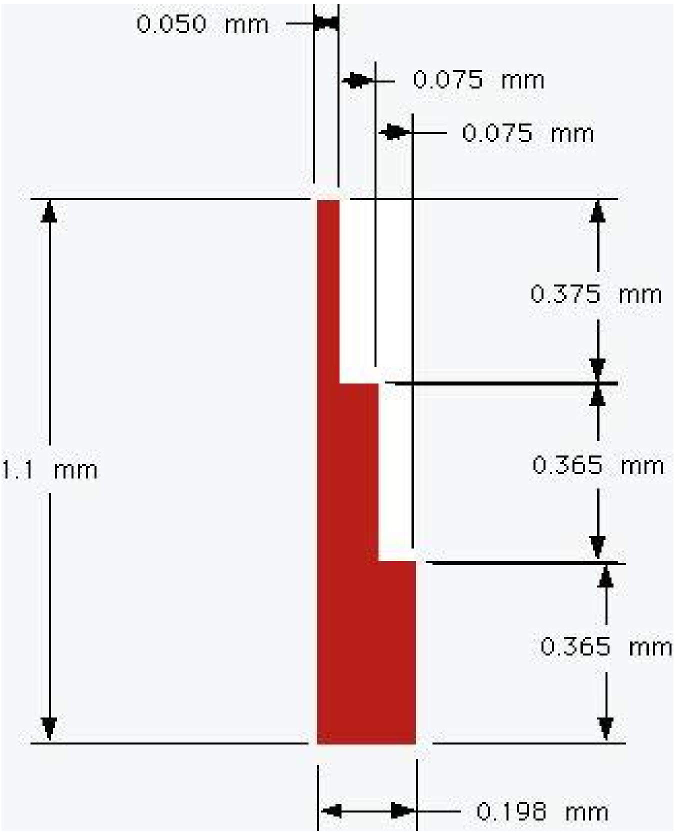

Figure 4.6: Dimensions of the stepped witness plate.

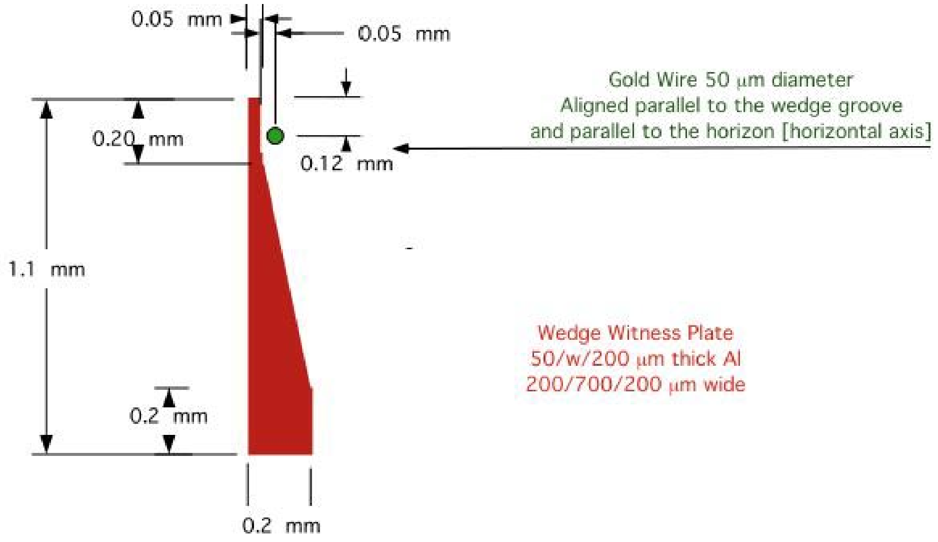

Figure 4.7: Aluminum wedge.

the edge of the exit hole could not effect the image at the step edges. The step edges were also meant to examine the spatial resolution of the total SOP diagnostic system. The data, displayed in Table 4.1, give a consistent shock speed of 57 ± 2 μm/ns across the first step, and 35.6 ± 0.5 μm / ns across the second step. This slowing down is predicted by calculations, Figure 4.10, shown later under the theoretical section. The edges were clearly resoved with a resolution of about 50 μm.

4.5 Shock velocity measurements using wedges

Two wedged aluminum targets were used in shots 13690 and 13694 with 45 beams. The wedges are used to give a continuous measure off the shock arrival time at the rear of the wedge. The disadvantage of using wedges is the variation of the strength of the shock with time, and the uncertainty about the absolute time in the arrival of the shock due to uncertainty in locating the wedge along the diagnostic hole. The shape of the wedge is shown in Figure 4.7. A wire was placed perpendicular to the slit of the streak camera to give a spatial fiducial, The slit of the streak camera was imaged in in the plane of the figure and sampled a 200-μm width of the wedge.

Figure 4.8 gives an example of a wedge output on the streak camera where time flows downward in the figure. The data shows two regions of emission. The emission at the left is due to wedge, with the wedge's thickness, and hence axial propagation distance, increasing towards the left of the figure. The emission shows a dip because we placed a gold wire to establish a spatial marker at the wedge surface. The gold wire blocks some of the light from the wedge, but eventually, the plasma and/or the radiation flow around the wire. The ramp

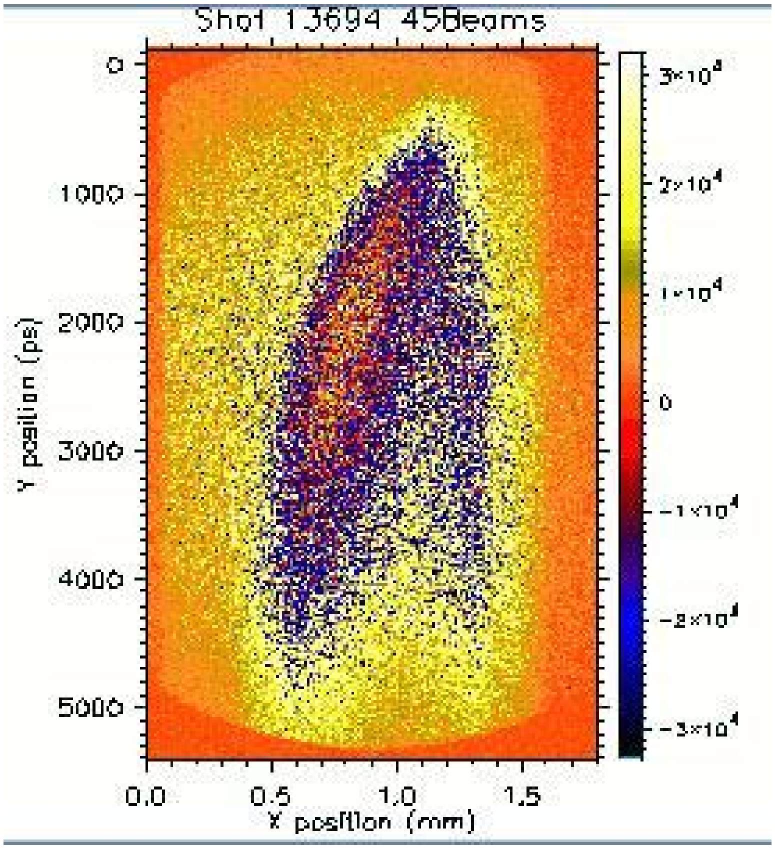

Figure 4.8: Streak camera record of emission.

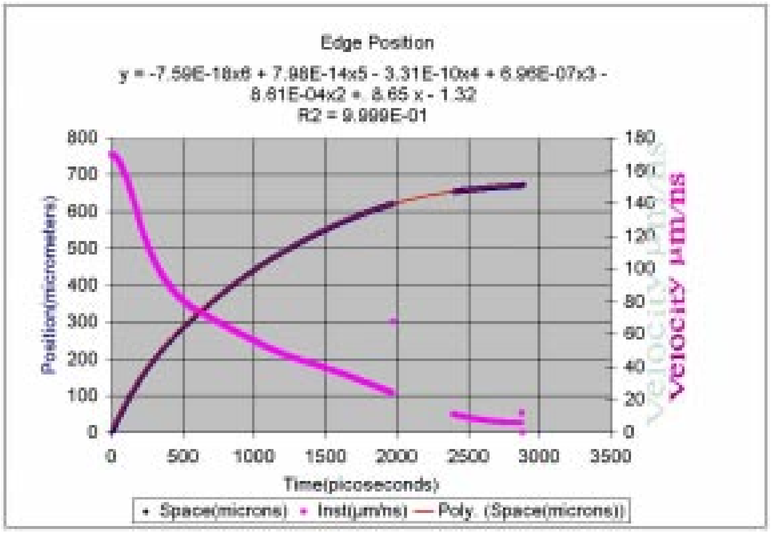

Figure 4.9: Measured shock velocity in aluminum.

data show the slowing down of the shock after it traversed only 50 μm of the base of the wedge. The slope of the emission gives a continuous measure of the velocity. Figure 4.9 gives a time history for shot 13694. The data was analyzed by finding the position where the signal was 10% of the peak value of the emission intensity, at each time. The position versus time, shown as a Nile-Blue color in Figure 4.9. The data were fit to a sixth-order polynomial, shown in red, and then analytically differentiated to give a final velocity. At early times,$<$ 500 ns, the error in the measurement of the speed is large due to the presence of the flat region of the wedge that we can not resolve well, and the weakness of the signal. This uncertainty also yields a fractional error in the time where velocity is measured. The error is largest at early times, and smallest at late times. We noticed that the emission had a sharp turn on and quick turn off in agreement with the two-dimensional Lasnex simulations shown in Figure 4.10. Emission is peaked for a time of order several hundred picoseconds after breakout. Since the slope of the wedge is 0.14, the calculated mean shock velocity over the first 1.2 ns after breakout is about 50 μm/ns.

4.6 Discussion of theoretical drive results

For calculations of shock velocity in the aluminum witness plate, the radiation drive was determined from Lasnex by using a one-dimensional spherical hohlraum calculation with P_n radiation transport, the appropriate laser deposition source, a term for laser entrance hole radiation losses, and an aluminum sphere at the hohlraum center with surface area equal to the surface area of the aluminum drive plate subtended by the defining hole in the hohlraum wall.

Then the radii of the hohlraum shell and the aluminum shell were scaled up in linear dimension by a factor of 10 so that convergence effects would be minimized for the shock

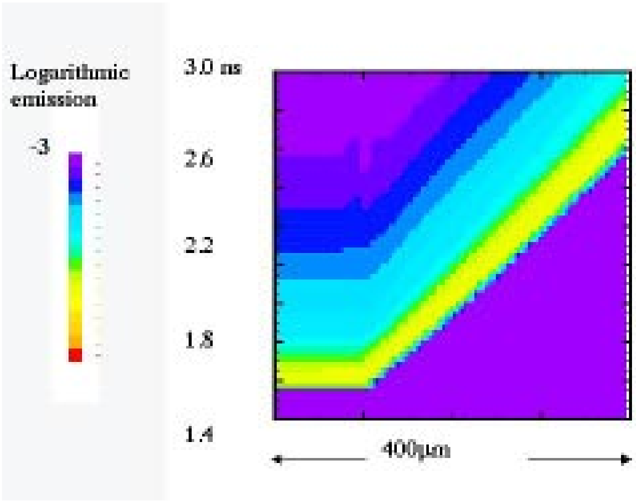

Figure 4.10: A Lasnex streak simulation of shock breakout emission from an aluminum witness wedge. The wedge runs left to right and the time of observation at the left.

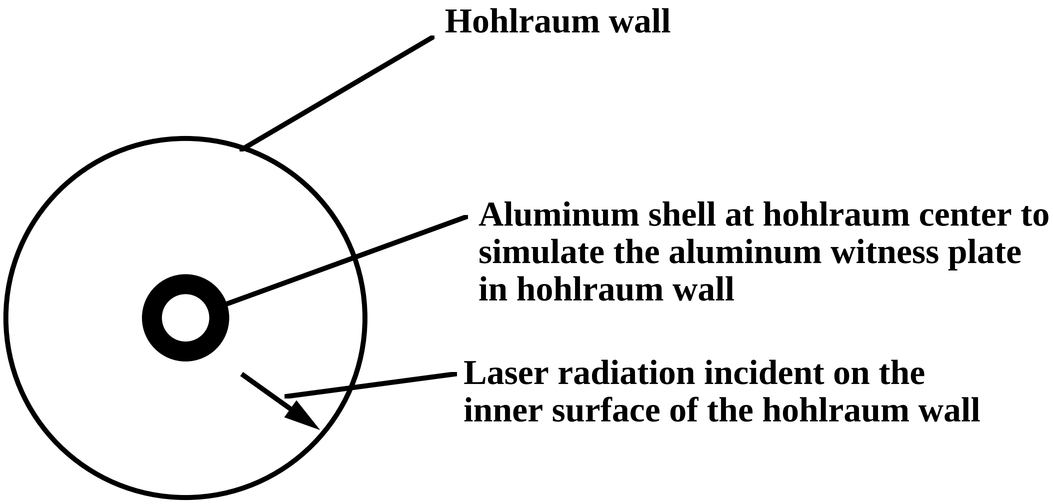

Figure 4.11: The geometry used for the calculations.

Table 4.2: Shock front displacements in microns as a function of time after the onset of the laser pulse for Rage and Lasnex calculations of aluminum targets in scale 1.2 tetrahedral hohlraums.

	1 ns	2 ns	3 ns	4 ns	4.6 ns
Rage	36	88	136	179	200
Lasnex	35	85	134	177	

Table 4.3: Shock front velocities ($\mu m/ns$) derived from the displacements of Table 4.2.

	0-1 ns	1-2 ns	2-3 ns	3-4 ns	4-4.6 ns
Rage	36	52	48	41	38
Lasnex	35	50	49	43	

in aluminum, and the density of material in the hohlraum between the aluminum sphere and the hohlraum shell was made extremely low to avoid making the hohlraum volume an erroneously large energy sink; correspondingly the incident laser energy and the energy loss due to the laser entry holes were increased by a factor of 100. Hence the shock motion in the aluminum sphere was determined as part of a single Lasnex calculation.

The hohlraum radiation temperature obtained from the Lasnex calculation was used as the source in a two-dimensional Rage calculation which modeled both a section of the hohlraum wall, and the aluminum witness plate mounted on it. There were no geometric convergence effects in the direction of shock propagation, although the two-dimensional modeling of the hohlraum wall chapter and the planar target allowed for the calculation of rarefaction effects due to the finite size of the aluminum witness plate surface transverse to the direction of shock motion.

The agreement between the Lasnex and Rage results as shown in Tables 4.2 and 4.3. indicates that geometric convergence effects in the Lasnex calculation are not significant. The calculated value for the shock speed at early times appears to be somewhat (about 10%) lower than the experimental result.

The experimental slowing of the shock with increasing time, as shown in Figure 4.12, appears to be somewhat greater than calculated. It is possible that the hohlraum drive on the witness plate is decreasing more rapidly than calculated. The resolution of these differences would further our understanding of the hohlraum behavior and the experimental procedures.

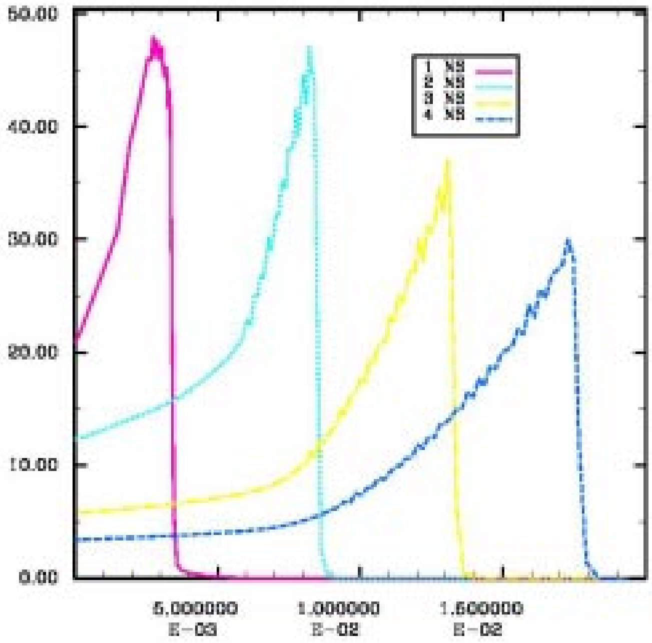

Figure 4.12: Pressure in Mbar as a function of position (cm) at times from 1 to 4 ns from the Lasnex calculation of the shock propagation in aluminum.

4.7 Results from structured targets

Only one shot, 13693, used a structured target. It consisted of an aluminum joint between two copper-doped beryllium flats. The emission did not show a distinct region or discontinuity across the joint. This could be either due to the lower than expected spatial resolution of the SOP diagnostic (design value is 10 μm spatial resolution, and 20 ps temporal resolution). Calculations, see Figure 4.13, indicate that there is a region of approximate width 25 micrometers where the shock front is advanced by 50 ps![10] The present resolution, or focusing, was not adequate to resolve these features.

4.8 Summary

We have successfully implemented the new SOP diagnostic to measure the drive in tetrahedrally illuminated spherical hohlraums. We have tested this diagnostic and found some limitations. We have also measured the spatial uniformity of the drive, and have seen some edge effects. We were not able to use the SOP to measure the shock breakout in a structured target, nor were we able to compare the results of SOP measurements with those from DANTE, a filtered x-ray diode.

For the future, we suggest: have targets built specifically to focus SOP in a real situation, have DANTE working in concert with the SOP, reduce the jitter in the streak camera, and obtain a better timing of the SOP streak camera with the 3ω fiducial fibers. Last, repeat the wedge measurements with a thinner wedge and with smaller angle so as to measure the early drive history more accurately.

4.9 Appendix: Preliminary Quick Post Shot report on Operations.

Text of LANL Memo sent as document LLE_POST_SHOT on 4 November 1998

Laser:

- Generally very good UVOT: more than the 21 kJ we expected, the energy varied from 20.8 to 23.8 kJ with an rms from 5.1% to an anomalous 14.3%.
- We wanted to use a 1 ns square pulse. The SG1011 pulse shape control was achieved, and we were informed of the expected shape prior to every shot. The pulse shape was not usually square, but it had a sloping shape and had three main peaks. The shape was acceptable for this preliminary experiment.
- One shot (13693) with 45 beams had problems with the rms value of the beams.
- Another shot (13663) with 60 beams had 23 kJ instead of the expected 30 kJ.

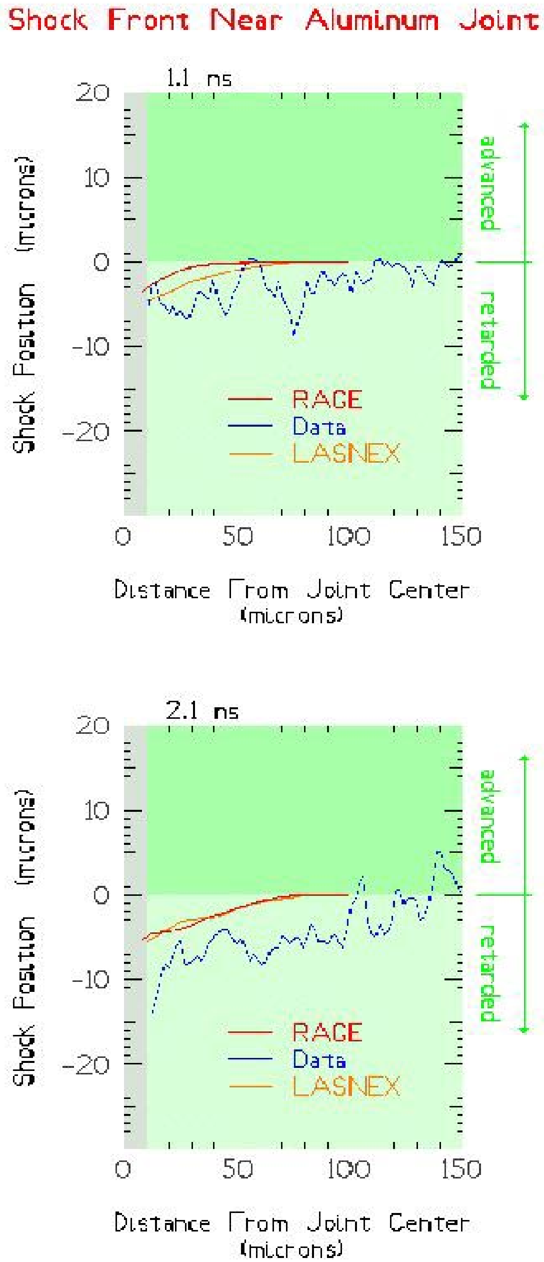

Figure 4.13: Joint calculation.

Primary diagnostics:

- We had major problems with Dante. Dante was not implemented correctly and we had trouble with the scopes. We must coordinate with previous users to leave the instrument in well defined conditions.
- The SOP worked on the first shot, and as time evolved, we managed to increase the signal levels. Refocusing and repointing were attempted, but spatial resolution was not sufficient for the joint experiment and needs to be redone before the next series. Instantaneous CCD results were very helpful in quickly adjusting the diagnostic. More signal and less pixellation need to be done before the series. Speed of the camera appears to be not consistent with fiducial readings on the P510 recording and needs be investigated.

Secondary diagnostics (x-ray imaging):

- The pointing (and timing) of the XRFCs appears to OK; after adjustments over previous several shots they worked well. It would be useful to have better timing information for each diagnostic in each TIM (just like Nova and Trident with the SIM's and GXI's, x-ray streak cameras, etc.) so that diagnostic switches between TIM's can be better made.
- We attempted to use the IXRSC, but failed to get it running. It would be a useful instrument to use by making the slit rotatable and adjustable. This allows the user to look at the spectra from within the hohlraums.
- Most of the cameras worked fine. There were some small problems with x-ray diagnostics:
  - 4× pinhole camera located in H13C appeared to have a problem with the Al filter, the image was partly obstructed with an opaque part of the filter.
  - Some 4× pinhole images seem to have had their film marked with circular rings.
  - some random artifacts appear on film; possibly electrostatic effects?

Targets:

- Most of the targets were fine; one had to be discarded because the holes were way off. The pictures were informative; it would be nice to record the view of target as mounted using the sun system at OMEGAs' target assembly facilities.
- The conical shield worked great. We did not see scattered light in the SOP, and the laser beams did not hit the shields.

Positive feedback:

- I am happy with film in the cameras. Most of the pointing was correct and did not necessitate any changes between shots. CCDs would be great on 4× cameras to speed readout, and confirm alignment.
- Beam pointing and timing appeared outstanding!
- The diagnostic monitor system seemed to work quite well for timing the cameras.
- Target alignment went very smoothly and the alignment crew were patient with us.
- Laser performance (energy quantity, pulse shape control, and pointing) was very good, although better energy balance would be beneficial towards optimum hohlraum drive symmetry. During the shot day, 5.1% - 14.3% rms energy balance was achieved.
- Laser pulse shape control needs some more time ahead of the experiment.
- The Powell scope worked wonderfully, allowing for rechecking of target metrology on site.
- The on-line shot request form application is frustrating, it is slow, does not allow copy and paste. Help from the computing staff was most welcome and appreciated especially when they observed how we interacted with the system. They experienced the same frustration we did. I suggest scrapping any server-based system and accepting excel spreadsheets instead. We had the same frustrating time with Livermore's painfully slow 4D system. I easily spent 6 hours to put the sheets in form, something I could have done in few minutes in Excel.
- A new unscratched absolutely calibrated P11 wedge would be very helpful. Also an absolutely calibrated P20 would be most welcome.
- The LLE staff have been very helpful and supportive of our experiments, and we gratefully appreciate it! Both the flexibility of the Omega staff, in adding a new diagnostic during the experiment, and the quality of the operation were fully appreciated.
- The turn around time when no film was developed was outstanding, less than 29 minutes before shots, that we finished early on Friday and I did enjoy a trip to the lake at sundown.

4.10 Dante results

Six SCD 5000 digitizing scopes were sent out to OMEGA the first week of Aug. and set up in preparation for this series of experiments.

The overall success of recording data for this series was marginal at best. We found out late in the week that the DANTE detector array had been modified for the University of Wisconsin experiments which were run the week of Aug. 31. It is not clear that the diagnostic was returned to it's original configuration after this series of shots. The difficulties we encountered are noted as follows.

The computer in LaCave is dying a slow and ugly death. We had to replace the power supply as soon as we arrived. The arming command is becoming unreliable. If we leave the scope mode, go to DOS, and return, we must cycle through at least 6 gpib error reads before the scopes will arm.

As a general practice, the SCD scopes are set up such that a fiducial time mark and two signal channels are recorded on one scope. In this way, we can record 10 channels on five scopes. The "standard" setup is to record channels 1 and 6, 2 and 7, 3 and 8, 4 and 9, 5 and 10 each as a pair, and a fidu "fills" 20 ns of time window. A memo from Bob Turner suggested that we record the lower numbered channel later in time in order to avoid overlap of signals (i.e. ch. 6 would appear first on the scope, then channel 1, etc.). This requires that a time delay cable be added to the signal one wishes to have show up later in time. We found the cabling set up with the delay cables added to the lower channels as this would suggest. Early in the week, we spent a great deal of time trying to manage signal amplitude. We finally realized what the situation was when we started unplugging signal cables and isolating each signal as it came in. In as much as we now had a signal overlap as cabled, it was apparent that the alternative would be to put the delay cables on the higher numbered signal cables, and record in a 50 ns window. This would have decreased resolution, which was difficult to accept since several of the detectors were low in amplitude to begin with.

In addition, channels 1 and 3 were so far out of range in amplitude that we could not get them on scale with as much as 400× padding. We finally removed channels 1 and 3 from the digitizers. We suspect that those channels are damaged (burned or otherwise damaged filters). This should be checked out before the next series of measurements are made.

In summary, we believe the measurements did not meet the need of the experiment because: (1) two channels per shot were eliminated, and (2) we still had signal overlap.

4.11 Turner explanation of Dante results

I think I can reconstruct what happened to Dante.

- For the pointing shot: these are typically much lower energy than a full system shot on a hohlraum. The Dante needs to be run near max sensitivity, especially on the harder (higher number) channels, to see anything. The scopes, as left from the previous week, were set up correctly; but since attenuators were already in place for the expected hohlraum signals, the higher channels' signals were in the noise.
- This was mis-interpreted as NO early signals, and the scopes were delayed 10 ns (and the fidu too, I presume). This delay now causes the "late" signals (channels 1-5) to come near the start of the trace.

- At about 20 ns after t=0, the scopes start seeing extraneous signals. What's happening is that the early signals are running "backwards" thru the fidu cables, back to the splitters, and then "forward" thru the fidu cables to all the other scopes. So with too much delay on the scopes, you will see the "late" channels first, followed by a melange of overlapping signals from 4 "early" channels (which now the scope is triggering too late to see at the proper time). The attenuation will seem funny, since these late signals are a combination of channels.

- If channels 1 and 3 were properly identified and are that high, there must have been some sort of vacuum accident, or a target with massive shrapnel, which affected the filters. They worked okay the previous week, and were inspected at the end of the week. Perhaps they were damaged in re-inserting and pumping down.

Chapter 5

A Multipurpose TIM-Based Optical Telescope for the Omega and Trident Laser Facilities[11]

In the inertial confinement fusion (ICF) program, optical diagnostics have been important instruments for the measurement of laser plasma instabilities, direct-drive laser imprint, neutron burn history and radiation drive. Our primary motivation for designing and building an optical telescope was to measure the radiation drive temperatures in a tetrahedral hohlraum.[12] Hohlraum temperatures for inertial confinement fusion can reach temperatures exceeding 200 eV, pressures of 100 Mb and have been measured by several methods.[13] One of the most precise and technically mature methods of measuring radiation temperature is by streaked optical pyrometery, a technique that has been around for nearly twenty years.[14,15]

In this measurement technique, laser radiation drive interacts with the hohlraum wall and launches a shock wave. A section of the hohlraum wall is cut out and replaced with a wedged or stepped low-Z witness plate, usually aluminum. The shock-heated witness plate emits a flash of light that breaks out with a velocity relative to the hohlraum temperature as $T_R = 0.0126 v_s^{0.63}$ where T_R is the hohlraum temperature and v_s is the shock velocity.[13] The brief flash of light from the witness plate is imaged and magnified onto the slit of a streak camera, with an optical fiducial added for timing.

Although our primary reason for constructing this telescope is to measure a hohlraum temperature, we also want to have a flexible instrument that can be used for any experiment requiring high resolution imaging of optical radiation from 200 nm to 1 μm. An overall layout of the telescope and other hardware is shown in Figure 5.1. The text below is organized into four chapters. Section 5.1, details the optical telescope and how the optical cell interfaces into an Omega Ten-Inch Manipulator (TIM). Section 5.2, discusses the components outside the vacuum chamber including the optical table, final focusing optics, filters, and the streak camera. Section 5.3 briefly mentions system performance, overall specifications and alignment.

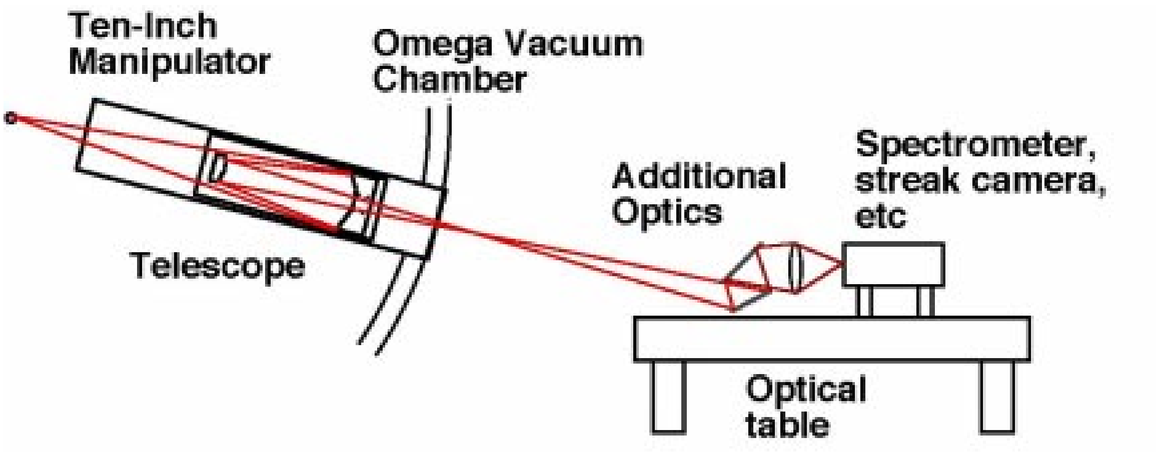

Figure 5.1: A generic layout of the optical telescope on the Omega target chamber.

5.1 The telescope

The TIM insertable f/7 telescope is based on a Burch[16] reflecting microscope design and has the advantage that all optical surfaces are spherical and thus has minimal aberrations. The six TIMs, located around the Omega target chamber, allow researchers the flexibility to place a variety of diagnostics inside the vacuum chamber without having the diagnostics permanently fixed. The telescope optical elements are mounted in a 90-cm long cylindrical optical cell which has a conical light shield, a removable alignment pointer, and is attached to a TIM boat by a three-point kinematic mount. See Figure 5.2. The TIM-boat, a permanently mounted fixture inside the TIM, travels into the target chamber and can be located anywhere along the TIM axis to an accuracy of 25 μm. As seen in Figure 5.3, the optical elements of the telescope consist of a blast shield, meniscus spherical corrector lens, primary mirror, and secondary mirror. The 90-mm diameter, 12-mm thick blast shield is located 450-mm from target chamber center (TCC) and has a 3ω (351-nm) rejection filter coating on the rear surface. The meniscus lens, designed to remove spherical aberrations induced by the flat blast shield, is 90-mm in diameter, has a thickness of 16-mm, and has both surfaces with a radius of 742-mm. Because it has zero power, it introduces negligible color aberrations. All of the transmissive optics in the system, including the blast shield and the meniscus lens, are made of a high quality fused silica to transmit UV light. The primary and secondary mirrors are made of ZERODUR,[17] are separated by 544 mm, and have a UV enhanced aluminized surface coating. This allows alignment at visible wavelengths while maintaining high reflectivity at 280 nm. The concave spherical primary mirror is 160-mm diameter, 25-mm thick, has a center hole clear aperture of 40-mm, and a radius of curvature of 825-mm. The convex spherical secondary mirror is 40-mm diameter, 23-mm thick, 278-mm radius of curvature, and is cemented to the convex-side of the meniscus lens. Light from the object plane comes out of the telescope nearly collimated, passes through a high quality quartz vacuum window at the rear of the TIM, and enters a light-tight enclosure mounted on the East wall of the Omega target bay. The window on the rear of the TIM also has a 1ω (1.053-μm) rejection filter to reduce unwanted, unconverted laser light.

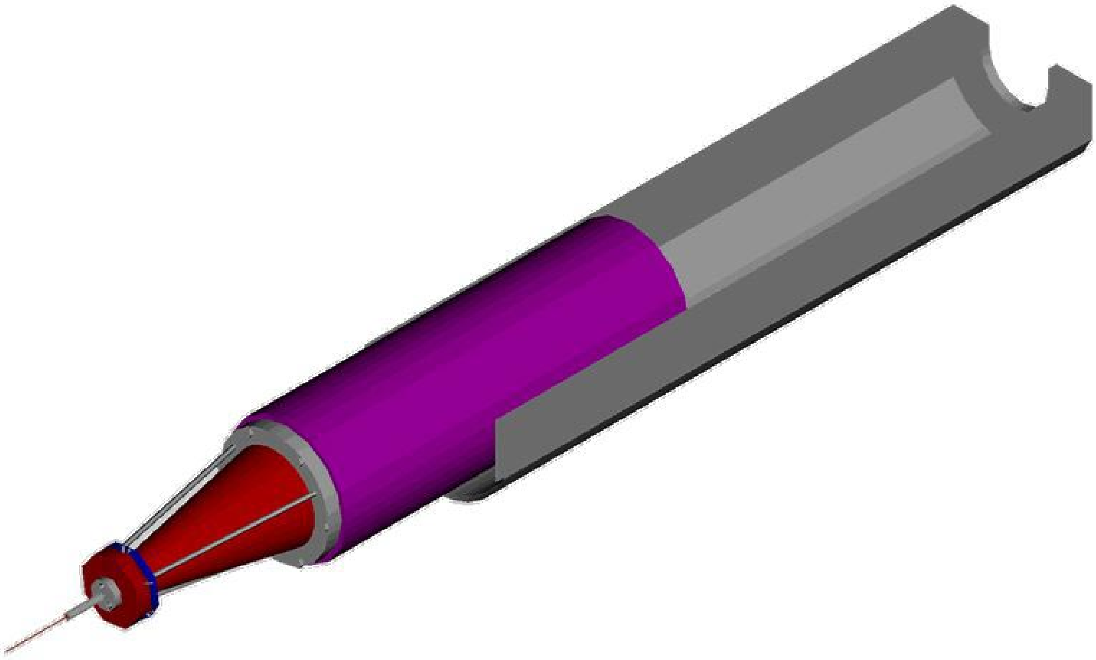

Figure 5.2: Optical cell with alignment pointer inserted into a TIM-boat.

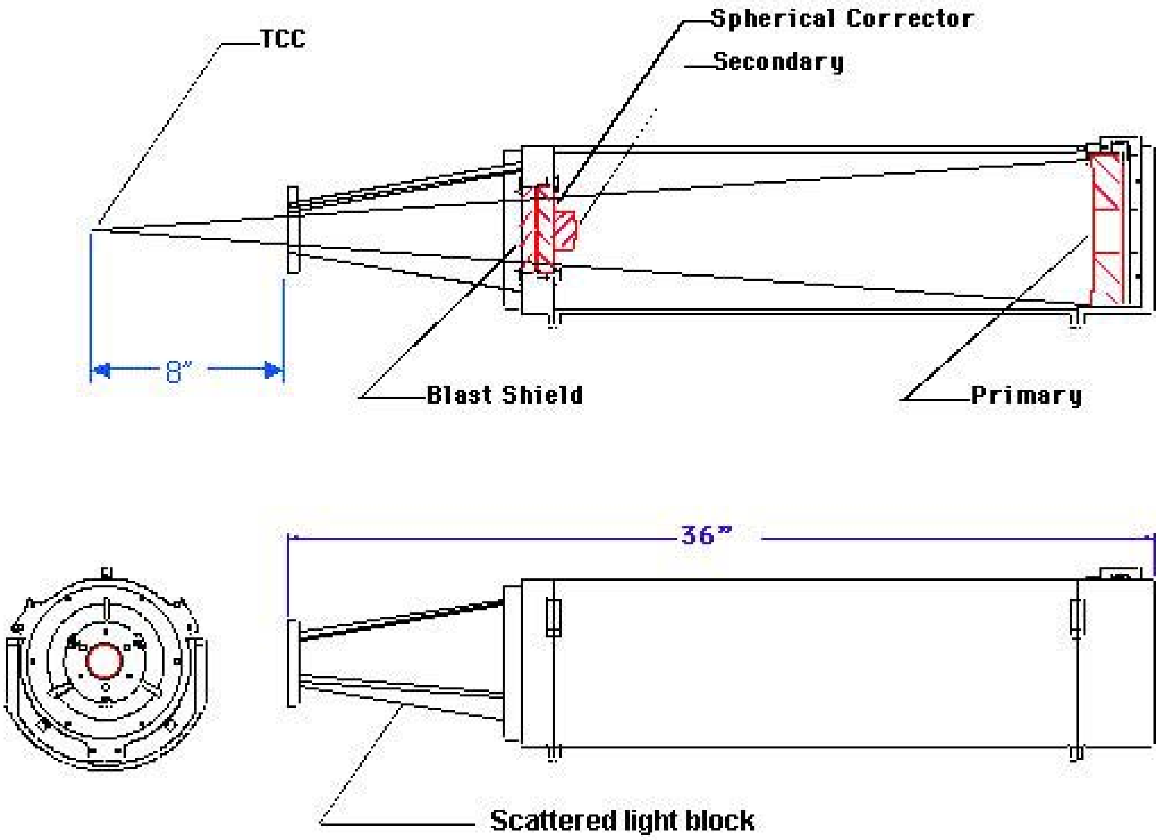

Figure 5.3: A cross-section and assembly view of the optical cell.

5.2 Components outside the chamber

The components outside the vacuum chamber include the optical table, final focusing mirrors, image rotator, filters, streak camera, CCD camera, and optical fiducial system. For our hohlraum temperature measurements, a 3'× 6' optical table and enclosure are mounted vertically on the Omega target bay East wall. The light-tight enclosure built around the table has a small hole to allow light to enter from TIM-5. The Omega target bay has an open-beam-transport architecture, so there are copious amounts of scattered 2ω (527-nm) light to filter out. Rejection is accomplished with a filter on the entrance of the light-tight table enclosure. A schematic of the optical table with components is shown in Figure 5.4. After the collimated beam comes into the enclosure, an un-obscured spherical telescope focuses the light to the image plane at the slit of a streak camera. The first spherical mirror is concave with a 5,407-mm radius of and 160-mm diameter. The second sphere, 1,000-mm from the first, has a 33,807-mm convex radius, and is 125-mm diameter. This focusing spherical telescope gives a magnification of 11.7× at the image plane. If a future experiment requires a different magnification than that provided by this spherical mirror combination, it is simple to modify the system. By changing out just these two final focusing mirrors, the magnification can be modified and the telescope inside the vacuum chamber is undisturbed. Because we want to perform a rotational scan of the witness plate, an image rotator is located after the final focusing mirrors. This "K" mirror, the reflective equivalent to a Dove prism,[18] has a set of three mirror surfaces arranged 60 deg of each other. Rotation of the "K" mirror at a given angular rate causes the image to rotate at twice this rate. A filter holder mounted on a kinematic mount contains a 280 ± 25-nm bandpass and neutral density filters. At this same location, an alignment camera can fit into the mount to view the target back through the entire optical system. Finally, the image falls on a variable slit on a Hamamatsu C4187 large format streak camera with an S-20 photocathode. Interfaced to the streak camera is a Photometerics 1024 × 1024 CCD camera for final data acquision.

5.3 System performance and specifications

A broadband optical analysis has been performed using the optics code ZMAX,[19] including a modulation transfer calculation (MTF). The optical system design is shown to be nearly diffraction limited at 280-nm in Figure 5.5. Even though the optical system is capable of spatial resolution $\geq$ 30-lp/mm at the image plane, the streak camera limits the entire system to 10.9-lp/mm.[20] The f/7, 11.7× magnification, system has a field of view of 6-mm and is limited by the 50-mm aperture in the TIM vacuum window. Mirror reflectivity and transmissive optics allows visible light from 200-nm to 1-μm, although for our temperature measurements, bandpass and notch filters have been included to limit the spectrum. The temporal resolution of the Hamamatsu streak camera is specified by Hamamatsu to be 6.8-ps FWHM and has been verified by tests at LANL's Trident short-pulse laser.

Rough alignment of the telescope is performed with a precision ground pointer mounted on the end of the conical light shield that is aimed at TCC and viewed with the Omega target viewing system. Once roughly aligned, an alignment Helium-Neon (HeNe) laser is inserted

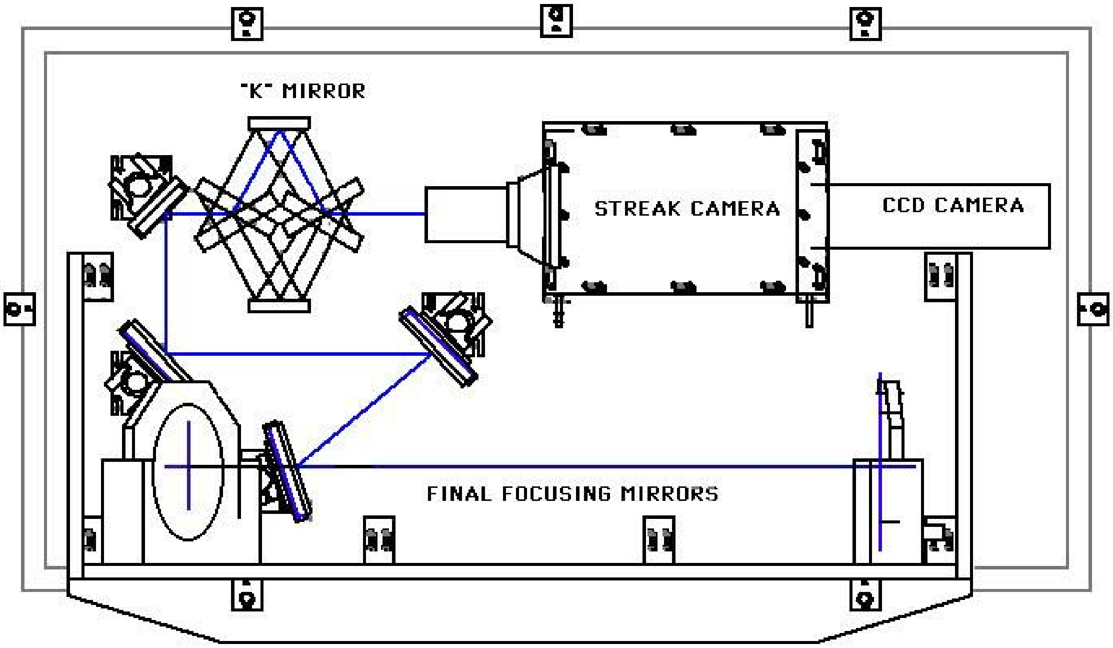

Figure 5.4: The optical table attached to the East wall with components.

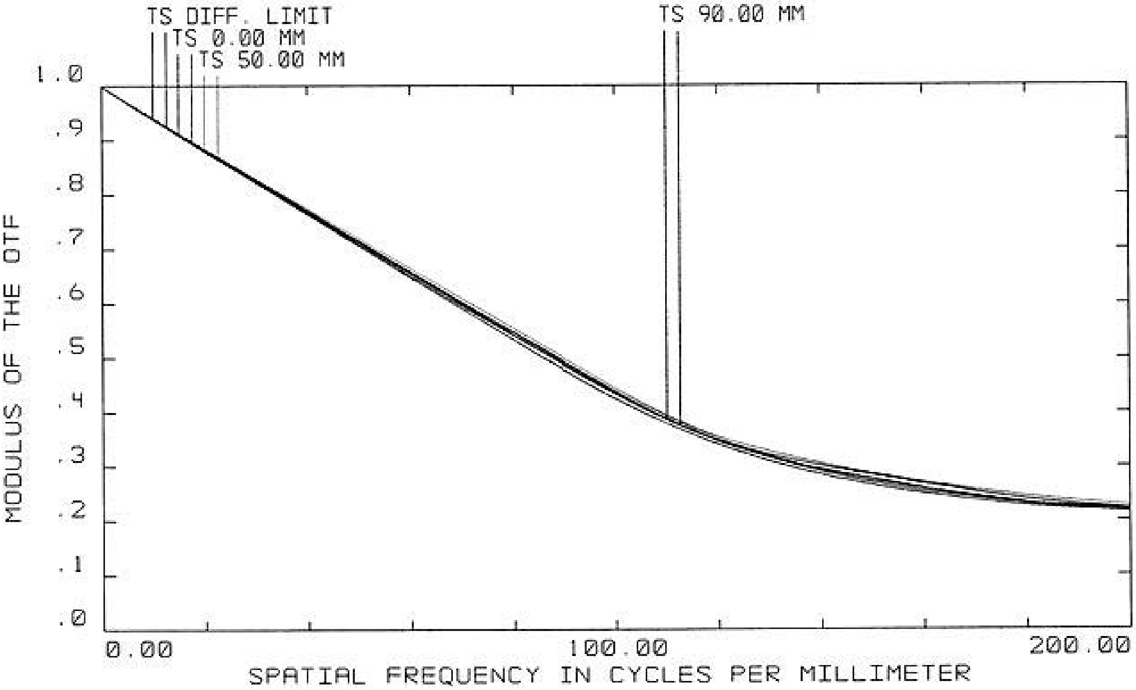

Figure 5.5: The modulation transfer function as measured at the image plane for 280 nm.

into the opposing TIM-3 with the beam pointed through TCC and out the backside of TIM-5. This permits alignment of the optics on the table with visible light. If an opposing TIM is not available, then a linear fiberoptic array will be placed at TCC. The array is relayed through the system and viewed at the image plane with a video camera. This also gives the rotational orientation requirements for the witness plate hohlraum experiments.

References

[1]C. Decker, R. E. Turner, O. L. Landen, L. J. Suter, P. Amendt, H. N. Kornblum, B. A. Hammel, T. J. Murphy, J. Wallace, N. D. Delamater, P. Gobby, A. A. Hauer, G. R. Magelssen, J. A. Oertel, J. Knauer, F. J. Marshall, D. Bradley, W. Seka, and J. M. Soures, Hohlraum radiation drive measurements on the Omega laser,*Phys. Rev. Lett.* **79**, 1491 (1997).

[2]T. J. Murphy, J. M. Wallace, N. D. Delamater, Cris W. Barnes, P. Gobby, A. A. Hauer, E. Lindman, G. Magelssen, J. B. Moore, J. A. Oertel, R. Watt, O. L. Landen, P. Amendt, M. Cable, C. Decker, B. A. Hammel, J. Koch, L. J. Suter, R. E. Turner, R. J. Wallace, F. J. Marshall, D. Bradley, R. S. Craxton, R. Keck, J. P. Knauer, R. Kremens, and J. D. Schnittman, Hohlraum symmetry experiments with multiple beam cones on the Omega Laser Facility, *Phys. Rev. Lett.* **81**, 108 (1998).

[3]T. J. Murphy, J. M. Wallace, N. D. Delamater, Cris W. Barnes, P. Gobby, A. A. Hauer, E. L. Lindman, G. Magelssen, J. B. Moore, J. A. Oertel, R. Watt, O. L. Landen, P. Amendt, M. Cable, C. Decker, B. A. Hammel, J. Koch, L. J. Suter, R. E. Turner, R. J. Wallace, F. J. Marshall, D. Bradley, R. S. Craxton, R. Keck, J. P. Knauer, R. Kremens, and J. D. Schnittman, Indirect drive experiments utilizing multiple beam cones in cylindrical hohlraums on OMEGA, *Phys. Plasmas* **5**, 1960 (1998).

[4]T. J. Murphy, J. Wallace, K. A. Klare, J. A. Oertel, C. W. Barnes, N. D. Delamater, P. Gobby, A. A. Hauer, E. Lindman, G. Magelssen, O. L. Landen, P. Amendt, C. Decker, L. Suter, B. Hammel, R. Turner, R. Wallace, R. S. Craxton, F. J. Marshall, D. Bradley, D. Harding, K. Kearney, R. Keck, J. Knauer, R. Kremens, W. Seka, M. Cable, and J. Schnittman, Experiments utilizing spherical hohlraums with tetrahedral illumination on Omega, *Bull. Am. Phys. Soc.* **42**, 2008 (1997).

[5]J. M. Wallace, T. J. Murphy, N. D. Delamater, K. A. Klare, J. A. Oertel, G. R. Magelssen, E. L. Lindman, A. A. Hauer, P. Gobby, J. D. Schnittman, R. S. Craxton, W. Seka, R. Kremens, D. Bradley, S. M. Pollaine, R. E. Turner, O. L. Landen, D. Drake, J. J. MacFarlane, Inertial Confinement Fusion with Tetrahedral Hohlraums at OMEGA, *Phys. Rev. Lett.* (to be published).

[6]J. D. Schnittman, R. S. Craxton, Indirect-drive radiation uniformity in tetrahedral hohlraums, *Phys. Plasmas* **3**, 3786 (1996).

[7]D. W. Phillion, S. M. Pollaine, Dynamical compensation of irradiation nonuniformities in a spherical hohlraum illuminated with tetrahedral symmetry, *Phys. Plasmas* **1**, 2963 (1995).

[8] T. J. Murphy, Tetrahedral Hohlraum Proof-of-Principle Experiments on Omega ID2, March 24-28, 1997 (unpublished).

[9] T. J. Murphy, Tetrahedral Hohlraum High-Convergence Implosion Experiments on Omega, ID4-FY98, August 31-September 4, 1998, LA-UR-98-4056.

[10] S. R. Goldman, S. E. Caldwell, M. D. Wilke, D. C. Wilson, Cris W. Barnes, W. W. Hsing, N. D. Delamater, G. T. Schappert, J. W. Grove, E. L. Lindman, J. M. Wallace, R. P. Weaver, A. M. Dunne, M. J. Edwards, P. Graham, and B. R. Thomas, Shock structuring due to fabrication joints in targets, submitted to *Phys. Plasmas*, (LA-UR-99-1768).

[11] J. A. Oertel, T. J. Murphy, R. R. Berggren, J. Faulkner, R. Schmell, D. Little, T. Archuleta, J. Lopez, and J. Valverde, Multipurpose 10 in. manipulator-based optical telescope for Omega and the Trident laser facilities, *Rev. Sci. Instrum.* **70**, 803 (1999).

[12] T. J. Murphy *et al.*, *Bull. Am. Phys. Soc.* **42**, 2008 (1997).

[13] R. L. Kauffman *et al.*, *Rev. Sci. Instrum.*, **66**, 678 (1995).

[14] R. J. Trainer *et al.*, *Phys. Rev. Lett.*, **42**, 1154 (1979).

[15] T. H. Lower *et al.*, *Phys. Rev. Lett.*, **72**, 3186 (1994).

[16] Michael Bass ed., Handbook of Optics, McGraw-Hill, NY, 1995.

[17] ZERODUR (R) is a registered trademark of Schott Glass Technologies Inc.

[18] J. H. Moore, C. C. Davis, M. A. Coplan, *Building Scientific Apparatus*, Addison-Wesley Publishing, 1989, 2nd ed., p. 152.

[19] ZMAX is an optical design and evaluation code made by Focus Software, Tuson, AZ.

[20] Information from Hamamatsu C4187 specification manual.